EARLY LIFE IMMUNOLOGY

Kupffer cell reverse migration into the liver sinusoids mitigates neonatal sepsis and meningitis

Bruna Araujo David[1,2], Jawairia Atif[3,4], Fernanda Vargas e Silva Castanheira[1,2], Tamanna Yasmin[5], Adrien Guillot[6], Yeni Ait Ahmed[6], Moritz Peiseler[6,7], Josefien W. Hommes[1,2], Lilian Salm[1,8], Marie-Anne Brundler[9], Bas G. J. Surewaard[1,2], Wael Elhenawy[10,11,12,13,14], Sonya MacParland[3], Florent Ginhoux[15,16], Kathy McCoy[17], Paul Kubes[1,2,5]*

In adults, liver-resident macrophages, or Kupffer cells (KCs), reside in the sinusoids and sterilize circulating blood by capturing rapidly flowing microbes. We developed quantitative intravital imaging of 1-day-old mice combined with transcriptomics, genetic manipulation, and in vivo infection assays to interrogate increased susceptibility of newborns to bloodstream infections. Whereas 1-day-old KCs were better at catching *Escherichia coli* in vitro, we uncovered a critical 1-week window postpartum when KCs have limited access to blood and must translocate from liver parenchyma into the sinusoids. KC migration was independent of the microbiome but depended on macrophage migration inhibitory factor, its receptor CD74, and the adhesion molecule CD44. On the basis of our findings, we propose a model of progenitor macrophage seeding of the liver sinusoids via a reverse transmigration process from liver parenchyma. These results also illustrate the importance of developing newborn mouse models to understand newborn immunity and disease.

INTRODUCTION

At birth, the immune system of neonates (1 to 28 days old in humans; 1 to 7 days old in mice) is fundamentally different from that of adults (*1*). This results in notable differences in susceptibility to bloodstream infections in neonates. Approximately 2 million children younger than 5 years old die annually because of infections, and, astoundingly, 50% of these deaths occur in neonates (*2*, *3*). After the neonatal stage, mortality rates due to infections strongly decline, suggesting a fundamental change in the immune system (*4*). Two major bacterial species, *Escherichia coli* (*E. coli*) and Group B *Streptococcus* (GBS; *Streptococcus agalactiae*), account for most neonatal infection cases that manifest as bloodstream infections (sepsis) and lead to meningitis (*5*), although other pathogens also can contribute. Whereas there is a prophylactic treatment for GBS (*6*), there is no preemptive therapy available for *E. coli*, in part because there are innumerable serotypes and because this ubiquitous bacterium is harbored by the human commensal microbiome. Antibiotics are used to treat *E. coli* infections in newborns, but a prophylactic administration to all newborns would (i) destroy critical commensal microbial flora (*7*), (ii) cause long-lasting alterations in immunity (*8*, *9*), and (iii) make infants more susceptible to infections after termination of antibiotics (*10*).

Despite the infection rate differences between neonates and adults, very few investigations have been performed in newborn humans or mice. Bloodstream infections have been investigated extensively in adult mice, and intravenous administration of *E. coli* and many other bacterial strains does not result in equal dissemination to all organs. First-pass clearance of blood-borne *E. coli* occurs within the liver, limiting dissemination to other organs (*11*). Intravital microscopy has identified a population of liver-resident macrophages called Kupffer cells (KCs) that reside within the sinusoids and sequester almost all bacteria flowing within the bloodstream (*12*, *13*). This vital contact of bacteria to the KC surface allows for subsequent phagocytosis that is mediated by canonical complement and unidentified immunoglobulin receptors (*11*, *13*). Specific removal of KCs from the sinusoids of adult mice leads to uncontrolled bacterial dissemination and increased mortality (*14*, *15*). As such, the intravascular location of KCs is critical for preventing bloodstream bacterial dissemination to other organs.

KCs develop from erythromyeloid progenitors (EMPs) that invade and colonize the fetal liver around embryonic day 8.5 (E8.5) onward (*16*, *17*). These EMPs located in the liver parenchyma undergo a coordinated differentiation program that includes the upregulation of macrophage-specific transcription factors, chemokines, phagocytosis, and scavenger receptors (*17*). Many of these cells leave the fetal liver and seed several organs where they acquire tissue-specific phenotypes. In adults, the tissue-specific signature of KCs includes the expression of the transcription factors *Nr1h3* (*Lxra*), *Spic*, *Id1*, and *Id3*, which can be traced back to as early as E10.5 (*16*–*18*). Similarly, in humans, progenitors from the yolk sac and the aorta-gonad-mesonephros colonize the fetal liver and give rise to

[1]Calvin, Phoebe, and Joan Snyder Institute for Chronic Diseases, Cumming School of Medicine, University of Calgary, Calgary, Alberta T2N 1N4, Canada. [2]Department of Physiology and Pharmacology, Cumming School of Medicine, University of Calgary, Calgary, Alberta T2N 1N4, Canada. [3]Department of Immunology, University of Toronto, Toronto, Ontario M5S 1A1, Canada. [4]Ajmera Transplant Centre, Toronto General Hospital Research Institute, University Health Network, Toronto, Ontario M5G 2C4, Canada. [5]Department of Biomedical and Molecular Science, Queen's University, Kingston, Ontario K7L 3N6, Canada. [6]Department of Hepatology and Gastroenterology, Charité–Universitätsmedizin Berlin, Berlin 13353, Germany. [7]Berlin Institute of Health (BIH), Berlin 10178, Germany. [8]Department of Visceral Surgery and Medicine, Inselspital, Bern University Hospital, University of Bern, Bern 3010, Switzerland. [9]Department of Pathology and Laboratory Medicine and Pediatrics, Cumming School of Medicine, University of Calgary, Calgary, Alberta T2N 1N4, Canada. [10]Department of Medical Microbiology & Immunology, Faculty of Medicine & Dentistry, University of Alberta, Edmonton, Alberta T6G 2E1, Canada. [11]Women and Children's Health Research Institute, University of Alberta, Edmonton, Alberta T6G 1C9, Canada. [12]Li Ka Shing Institute of Virology, University of Alberta, Edmonton, Alberta T6G 2E1, Canada. [13]Antimicrobial Resistance, One Health Consortium, University of Calgary, Calgary, Alberta T2N 1N4, Canada. [14]Striving for Pandemic Preparedness, Alberta Research Consortium, University of Alberta, Edmonton, Alberta T6G 2E1, Canada. [15]Singapore Immunology Network (SIgN), Agency for Science, Technology, and Research (A(*)STAR), Singapore 138648, Singapore. [16]Gustave Roussy Cancer Campus, Villejuif 94800, France. [17]Department of Microbiology, Immunology, and Infectious Diseases, Cumming School of Medicine, University of Calgary, Calgary, Alberta T2N 1N4, Canada.
*Corresponding author. Email: pkubes@ucalgary.ca

cells with a KC signature as early as 7 postconceptional weeks (PCW) (*19*, *20*). KCs reside in the fetal liver parenchyma and are distinct from the erythropoiesis-supporting VCAM-1$^+$, CD169$^+$, and erythropoietin receptor (EPOR)$^+$ erythroblastic island (EBI) macrophages also localized in the fetal liver parenchyma of both mice and humans (*20*, *21*). Given that the KC program is established before birth, KCs should be able to enter sinusoids to clear bloodstream bacteria. A previous study described KCs to be associated with sinusoids but more rounded and less ramified in the fetal liver than in adults (*22*). In this study, we imaged KCs in their neonatal environment and identified a critical parenchymal to intravascular relocation in the first few days after birth, which may explain the substantial increase in susceptibility to bloodstream infections and the considerable mortality in newborns.

RESULTS

E. coli sequestration by KCs is impaired in newborn mice

Among all organs, the liver has the largest population of resident macrophages (KCs) (*23*). These cells are an efficient filter, capturing pathogens directly from the bloodstream (*11*, *24*, *25*). To test whether the same pathogen clearance efficiency could be performed by newborn KCs, we challenged 1-day-old newborn mice with green fluorescent protein (GFP)–expressing *E. coli*, a pathogen responsible for high mortality rates in neonatal sepsis (*6*). First, we established the largest intravenous *E. coli* dose that was cleared from the circulation over time and did not induce mortality in adult mice [1×10^8 colony-forming units (CFUs)] (fig. S1A). To adjust the dose to a comparable infection in newborns, the CFU value was normalized and adjusted per body weight (fig. S1B). In vivo imaging revealed that bacteria reached the liver microcirculation at high speeds and were arrested/captured almost immediately in adults (Fig. 1, A and B, and movie S1). In stark contrast, 60% fewer bacteria were arrested in newborn livers (Fig. 1, A and B, and movie S2). Most *E. coli* were captured by KCs (defined as CD45$^+$CD19$^-$F4/80^{high}CD11b^{int}TIM4$^+$CRIg$^+$; fig. S1C) in both adults and newborns, but a much higher percentage of KCs caught *E. coli* in adults (83%) than in newborns (40%) (Fig. 1, C to E, and fig. S1, D and E). By contrast, less than 5% of *E. coli* in the liver was captured by neutrophils in both groups, with a slightly higher number of mature circulating neutrophils in newborns (fig. S1, F to H). Imaging also allowed for analysis of the number of bacteria caught per KC, which revealed that 65% of KCs in adults and 15% in newborns caught multiple bacteria (Fig. 1, D and E). We verified these results by flow cytometry, where no surgery or anesthesia was necessary before infection. In adults, the frequency of *E. coli*$^+$ KCs (defined as CD45$^+$CD19$^-$F4/80^{high}CD11b^{int}TIM4$^+$CRIg$^+$; fig. S1C) was double that of *E. coli*$^+$ KCs in newborns (Fig. 1, F and G).

Measuring bacterial burden in adult mice revealed that 70% of the bacteria injected were found in the liver 30 min after infection, compared with 35% in newborns (Fig. 1, H and I). In adult mice, the remaining bacteria that were able to bypass the liver were caught in the spleen and in the lung vasculature (fig. S1, I and J). As such, very few bacteria (10^2 of 10^8 injected or 0.0001%) reached the kidneys and/or brain, and these were further eradicated over 12 hours to undetectable levels in the brain and blood and fewer than 100 CFUs in the kidneys (Fig. 1, J and K, and fig. S1K). By contrast, in newborns, there was rapid dissemination to the brain, which increased ~2.5-log fold over the first 12 hours and coincided with increased levels of bacteria in blood (Fig. 1, J and K). Intravital microscopy of the brain meninges showed a similar increase. At 30 min, the bacteria were intravascular, whereas at 12 hours after infection, they could be seen in the parenchyma and often in CX3CR1$^+$ macrophages (Fig. 1, L and M). Whereas bacterial burden rose substantially in all organs of newborn mice, the increase in the brain was by far the greatest (Fig. 1, I to K, and fig. S1, I to K), consistent with the high susceptibility for meningitis observed in newborn humans. All newborn mice died in the first 24 hours after bacterial infection, whereas uninfected newborns and infected adult mice all survived indefinitely (Fig. 1N). Newborns succumbed to this concentration and even a 100-fold lower inoculum of *E. coli* (fig. S1A).

Considering that Gram-positive bacterial infections are also common in newborns and the increased burden of methicillin-resistant *Staphylococcus aureus* (MRSA) (*26*, *27*), we also tested the catching ability of KCs after MRSA infection. Similar to *E. coli*, *S. aureus* were efficiently captured by adult KCs, whereas in newborns, the number of bacteria arrested in the liver was considerably impaired (fig. S1, L and M). *S. aureus* was caught in the liver by KCs, with a higher percentage of bacteria-containing KCs in adults (60%) in comparison with newborns (20%) (fig. S1, N to P). In adults, KCs were found to internalize up to five bacteria per cell, whereas most KCs in newborns captured only one bacterium per cell (fig. S1, O and P). After *S. aureus* infection, all newborn mice died in the first 48 hours, with no mortality observed in adult mice (fig. S1Q). Together, these findings demonstrate that KC bacterial capture is impaired in newborns, leading to increased dissemination and higher mortality.

Lack of opsonins does not contribute to catching impairment by newborn KCs

To test whether a potential lack of natural antibodies and complement could explain the impaired catching of *E. coli* by newborn KCs, antibodies and complement that bound *E. coli* in the sera of adult and newborn mice were measured by flow cytometry. Unexpectedly, newborns had similar or higher levels of antibodies and complement factors in their sera compared with adults, with one exception: immunoglobulin M (IgM) (fig. S2, A to G). IgM is not maternally transferred and showed negligible levels in newborns, whereas adults had substantial amounts of this antibody (fig. S2G). To test whether the impairment in *E. coli* catching by KCs was due to a deficiency in bacterial opsonization by IgM, newborn mice were infected with *E. coli* incubated with phosphate-buffered saline (PBS) (naturally opsonized by their own newborn serum) or *E. coli* opsonized with adult serum. No differences were observed in the capture of adult serum–opsonized bacteria versus newborn naturally opsonized bacteria by KCs in newborns (fig. S2H). In addition, adult serum treatment did not reduce bacterial burden in the liver, brain, or blood 6 hours after infection in newborn mice (fig. S2, I to K), indicating that the presence of IgM does not improve *E. coli* capture by KCs or prevent dissemination in 1-day-old newborns.

Our group has previously reported that preimmunization could improve bacterial clearance by KCs in complement-deficient mice as young as 2 weeks of age and in adult complement-deficient mice (*11*). To test whether preimmunization with *E. coli* could improve bacterial catching by newborn KCs, adult female mice were preimmunized with heat-killed *E. coli* intraperitoneally before mating (fig. S2L). To confirm the transfer of anti–*E. coli* antibodies, the levels of IgG3 reactive against *E. coli* were measured in pups from immunized moms, showing a significant increase in comparison with newborn controls (fig. S2M). However, the higher levels of IgG3 reactive against *E. coli*

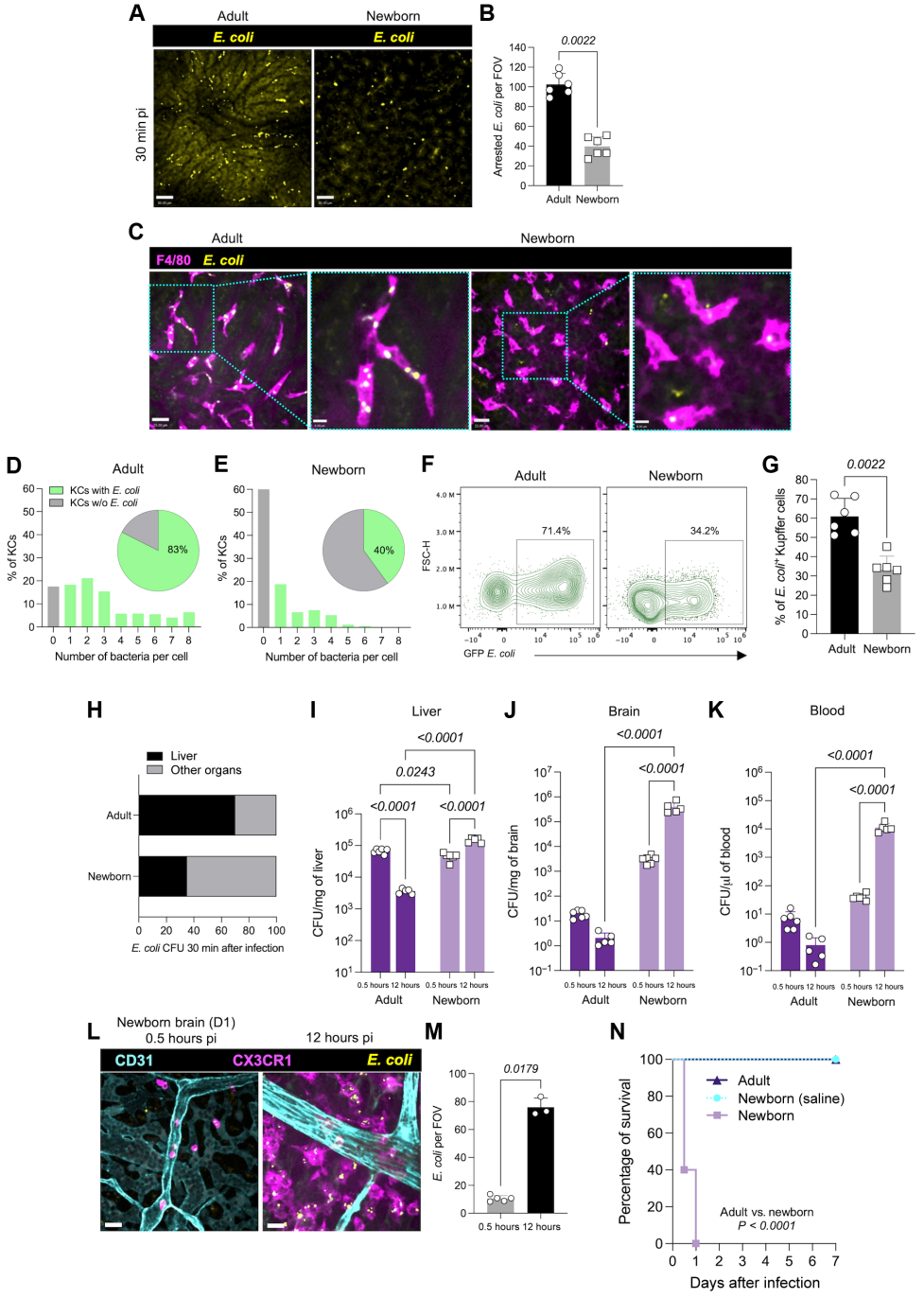

Fig. 1. *E. coli* sequestration by KCs is impaired in newborn mice. (**A**) Representative intravital microscopy (IVM) 30 min after GFP *E. coli* (yellow) challenge of adult and newborn mouse livers. Scale bars, 50 µm. (**B**) Quantification of (A) as *E. coli* arrested in the livers of adult and newborn mice ($n = 6$ per group, $N = 2$). (**C**) Representative IVM of GFP *E. coli* (yellow) caught by KCs labeled with F4/80 (magenta) in adult and newborn mice 30 min after bacterial challenge. Scale bars, 25 and 8 µm (zoom in). (**D** and **E**) Quantification of (C) as the frequency of KCs with internalized GFP *E. coli* in adult and newborn mice (pie chart). Number of *E. coli* per individual KC in adult and newborn mice (bar graph) ($n = 7$ or 8 per group, $N = 3$). (**F**) Representative flow cytometry pseudocolor plots of adult and newborn *E. coli*–infected mice gated on KCs. KCs were pregated as shown in fig. S1H. (**G**) Quantification of (F) as the frequency of KCs with internalized GFP *E. coli* in adult and newborn mice ($n = 6$ per group, $N = 2$). (**H**) Bacterial load in the liver and other organs combined 30 min after *E. coli* infection in adult and newborn mice ($n = 5$ or 6 per group, $N = 2$). (**I** to **K**) *E. coli* bacterial load in the livers, brains, and blood of adult and newborn mice 0.5 and 12 hours after *E. coli* infection ($n = 5$ or 6 per group, $N = 2$). (**L**) Representative brain IVM of newborns (D1) 0.5 and 12 hours after *E. coli* infection. Scale bar, 70 µm. (**M**) Quantification of (L) as *E. coli* per field of view (FOV) of newborn (D1) mice 0.5 and 12 hours after infection ($n = 3$ or 5 per group, $N = 2$). (**N**) Survival analysis of adult and newborn mice infected with 1×10^8 CFU *E. coli* normalized per 20 g of body weight ($n = 10$ to 15 per group, $N = 2$). Data are presented as individual values with the means ± SD. Mann-Whitney test was used for (B), (G), and (M). Two-way ANOVA with Šidák's posttest was used in (I) to (K). Kaplan-Meier test with Gehan-Breslow-Wilcoxon curve comparison was used in (N).

in the maternally immunized group did not affect the number of KCs, their location, or their efficiency in *E. coli* capture in the liver (fig. S2, N to P). This finding indicates that the bacteria, regardless of the presence of anti–*E. coli* antibodies or complement, were detected less efficiently by newborn KCs, suggesting an unknown underlying factor for impaired catching in newborns that may not be blood derived. For completeness, we used a public single-cell RNA sequencing (scRNA-seq) database (*28*) to assess the gene expression level of bacterial recognition and sensing receptors by KCs from day one (1 day old; D1) to adulthood (8 weeks old: D56) (fig. S2Q). The overall expression of the various phagocytic-related genes was similar among the age groups, with very few genes showing lower or higher expression in adults (fig. S2R).

Newborn KCs are morphologically distinct

Despite the vast number of studies on KCs, very little is known about these cells in newborns. Using a fate-mapping reporter mouse for Clec4f (*Clec4F*$^{cre\text{-}nTdTomato/+}$/*Rosa26*$^{ZsGreen/+}$), a type-C lectin identified as a specific marker for murine KCs (*29*), and intravenous injection of anti-F4/80 and anti–TIM-4 antibody, we were able to visualize bona fide KCs (Fig. 2A and fig. S3A). Unexpectedly, adult mice had fewer KCs than newborn mice (Fig. 2B). Moreover, the newborn KCs appeared more rounded and less polarized and had fewer ramifications. Three-dimensional (3D) reconstruction of newborn and adult KCs showed significant differences in cell morphology (Fig. 2C), with adult KCs having greater surface areas, volumes, and elongation and newborn KCs appearing smaller and more rounded (sphericity closer to 1) (Fig. 2, D to G). To investigate the same parameters in humans, preterm (22 to 30 PCW), full-term (37 to 40 PCW), and adult liver samples were obtained. In humans, liver macrophage (IBA1$^+$CD163$^+$ CD16$^+$) numbers were similar in adults and pre- and full-term newborns (Fig. 2, H and I). Evaluating the same morphological parameters, we found profound differences, with newborn macrophages being smaller and more spherical, consistent with our observations in mice (Fig. 2, J to L, versus E to G).

Adult and newborn KCs adopt distinct anatomical localizations

A key feature that KCs share in mice and humans is their strategic location, within the liver sinusoids in direct contact with the bloodstream. Intravital microscopy demonstrated the intravascular position of KCs in adult mice, where they cover a substantial portion of the sinusoidal lumen (Fig. 3A and fig. S3B), whereas intravital imaging of KCs in the D1 mice showed that the cells are still mostly outside the liver sinusoids in the perisinusoidal space (Fig. 3A and fig. S3B). Because it was not unusual to see adult KCs partially in and outside the vasculature (Fig. 3A, arrow heads) (*30*), we developed an image quantification protocol that assessed the percentage of sinusoidal lumen covered by KCs (fig. S3C). First, the surface area mask of blood vessels was created, and then the overlapping portion of KCs was superimposed onto the sinusoids to calculate the area of lumen covered by these cells (fig. S3C). Initial analysis of adult and D1 mice unveiled a notable difference in that KCs from D1 mice only covered ~6% of the sinusoidal lumen, whereas KCs from adult mice covered ~20% of the lumen (Fig. 3B). The percentage of lumen covered consistently increased over the first week, reaching ~20% at D7, with no additional increase at D21 or later (Fig. 3B and fig. S3D).

Recently, KCs were shown to extend out of the vasculature and make contact with hepatic stellate cells (HSCs), which is critical for KCs to establish their identity in adult mice (*30*). Using an HSC reporter mouse (*Lrat*^{cre}/*Rosa26*^{tdtomato}), we found that KCs do make contact with extravascular HSCs in adult mice (fig. S3E). The HSC-KC interaction was notable and perhaps even more extensive in newborns, where both cell types are in the same extravascular compartment (fig. S3F).

To examine whether newborn humans have a similar localization of liver macrophages as newborn mice, we obtained samples from humans of different ages and used the pan–macrophage markers CD163, IBA1, CD16, and collagen IV to delineate the basement membrane around the liver sinusoids (Fig. 3C). In the adult samples, macrophages were firmly within the sinusoids, covering ~20% of the sinusoidal lumen (Fig. 3, C and D). In pre- and full-term newborns, macrophages covered significantly less of the sinusoidal lumen (Fig. 3, C and D).

Next, we examined GFP *E. coli* capture in D1, D7, D21, and D56 mice. A minute-by-minute bacterial capture quantification (movies S1 to S4) showed that only the D1 mice had impaired *E. coli*–catching ability (Fig. 3E). The *E. coli* capture capability of KCs in D7 mice was similar to that in both D21 (movie S4) and D56 mice (Fig. 3E and movie S1), suggesting that increased lumen coverage by KCs in D7 and older mice had greater bacterial catching efficiency than the D1 KCs. The antimicrobial killing capacity of D7 mice was also closer to that of adults. Six hours after infection, liver bacterial burden suggested very effective killing of *E. coli* by adult mice, with similar killing efficiency in D7 mice but poor killing efficiency in D1 mice (fig. S3G). Similar *E. coli* elimination was observed in the brains of adult and D7 mice (fig. S2H).

Newborn KCs relocate to the intravascular compartment within 7 days postpartum

To track D1 perivascular KCs, we labeled the cells using a long-lasting tracer (blue CellVue cell linker) (Fig. 4A). Twenty-four hours after administering CellVue, 95% of the F4/80$^+$ KCs took up CellVue, suggesting efficient labeling of the perivascular cells (Fig. 4, B and C). This finding demonstrates that these perivascular KCs do have some access to the vasculature but have not yet fully translocated to the intraluminal space. This dye is retained by macrophages for up to 8 weeks, as previously shown (*31*). At D7 and even at D56, between 85 and 90% of the intravascular KCs retained CellVue (Fig. 4, B and C).

Because some CellVue does leak into other cells over 8 weeks, we also used a genetic approach to demonstrate that the D1 KCs in the parenchyma migrate into the vasculature at D7 and later. CX3CR1 inducible fate-mapping mice were used to track newborn KCs that at birth express CX3CR1 (fig. S4A) but are negative at D56. *Cx3cr1*^{creER}/*Rosa26*^{YFP} pregnant mice were treated with hydroxytamoxifen (OH-TAM), and the offspring were observed at D7 and D56 after birth (Fig. 4D). The vast majority (~90%) of intravascular KCs were YFP$^+$ and covered the lumens of sinusoids, identical to wild-type (WT) mice at D7 and D56 (Fig. 4, E and F).

The other possible seeding route of KCs is for monocyte progenitors to enter the liver directly via the vasculature and adhere in sinusoids. To examine this possibility, we used *Ms4a3*^{cre}-*Rosa26*^{TdTomato} mice, which report on monocyte-derived macrophages (*32*). Less than 5% of monocyte-derived KCs were detected at D7, followed by a very small increase in KC turnover observed in adult mice (fig. S4B), as previously shown (*32*), consistent with the view that most KCs in D7 mice were not derived from circulating monocytes. Dimensionality

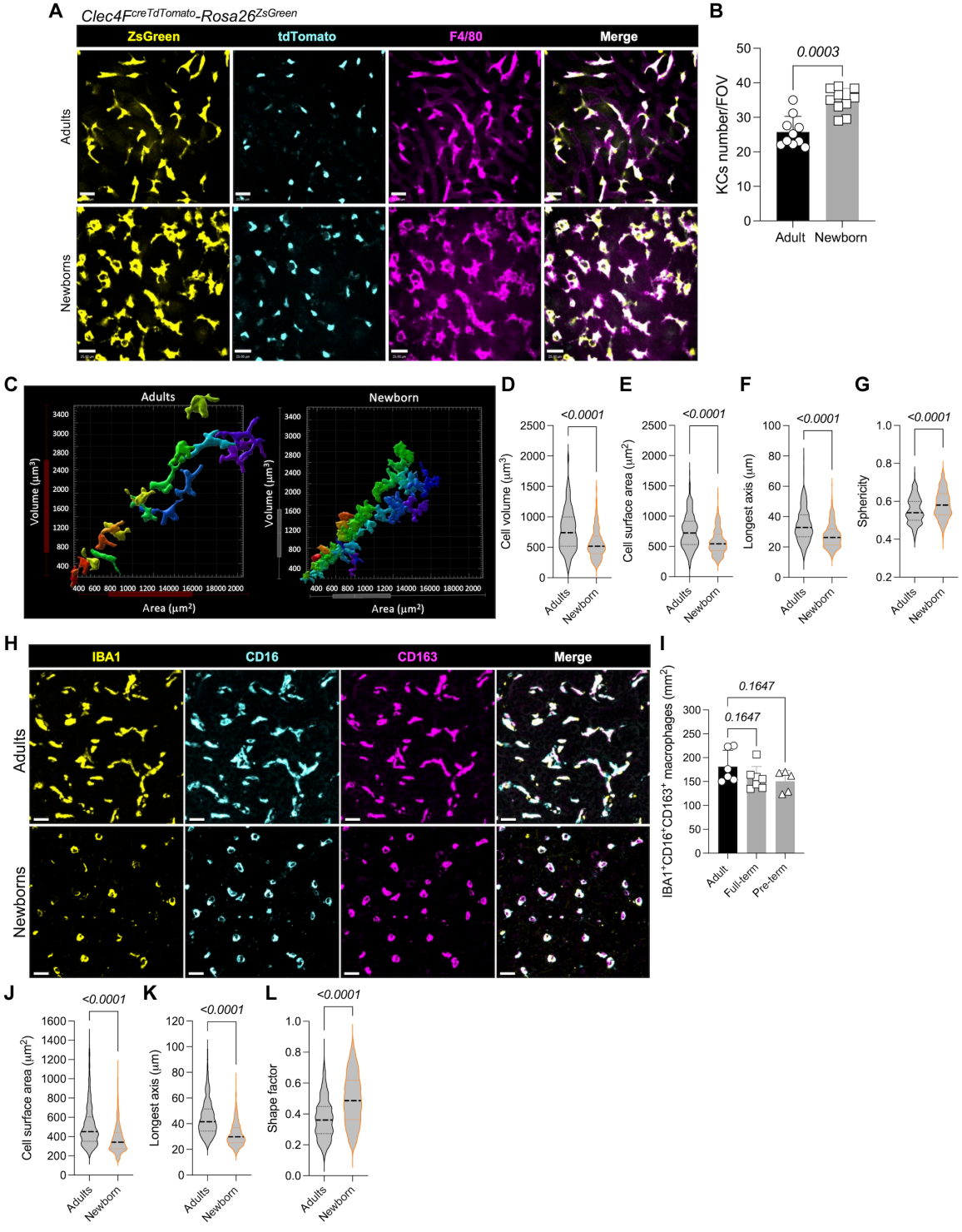

Fig. 2. Newborn KCs in mice and humans are morphologically distinct. (**A**) Representative IVM of liver showing bona fide KCs in Clec4F$^{-cre\text{-}nTdTomato/+}$ Rosa26$^{-ZsGreen/+}$ adult and newborn mice. Cytosolic Clec4F (Zsgreen; yellow) and nuclear Clec4F (tdTomato; cyan) combined with F4/80 (magenta). Scale bars, 25 µm. (**B**) Quantification of (A) as KCs per FOV in adult and newborn mice ($n = 10$ per group, $N = 3$ or 4). (**C**) Representative IVM with 3D reconstruction of adult and newborn KCs distributed on the basis of cell volume and surface area and color-coded by sphericity. (**D** to **G**) Quantification of (C) as the morphology parameters of cell volume, surface area, longest axis, and sphericity of KCs in adult and newborn mice ($n = 5$ per group, $N = 2$). (**H**) Representative immunofluorescence showing IBA1 (yellow), CD16 (cyan), and CD163 (magenta) in human livers. Scale bars, 25 µm. (**I**) Quantification of (H) as number of IBA1$^+$CD16$^+$CD163$^+$ cells (macrophages) per square millimeter ($n = 5$ to 7 per group, $N = 2$). (**J** to **L**) Quantification of (H) as the human liver macrophage morphology parameters comparing surface area, longest axis, and sphericity in adult and newborn mice ($n = 6$ for adults and $n = 12$ for newborns, $N = 2$). Data are presented as individual values with the means ± SD. Mann-Whitney test was used for (B), (D) to (G), and (J) to (L). One-way ANOVA with Dunnett's posttest was used for (I).

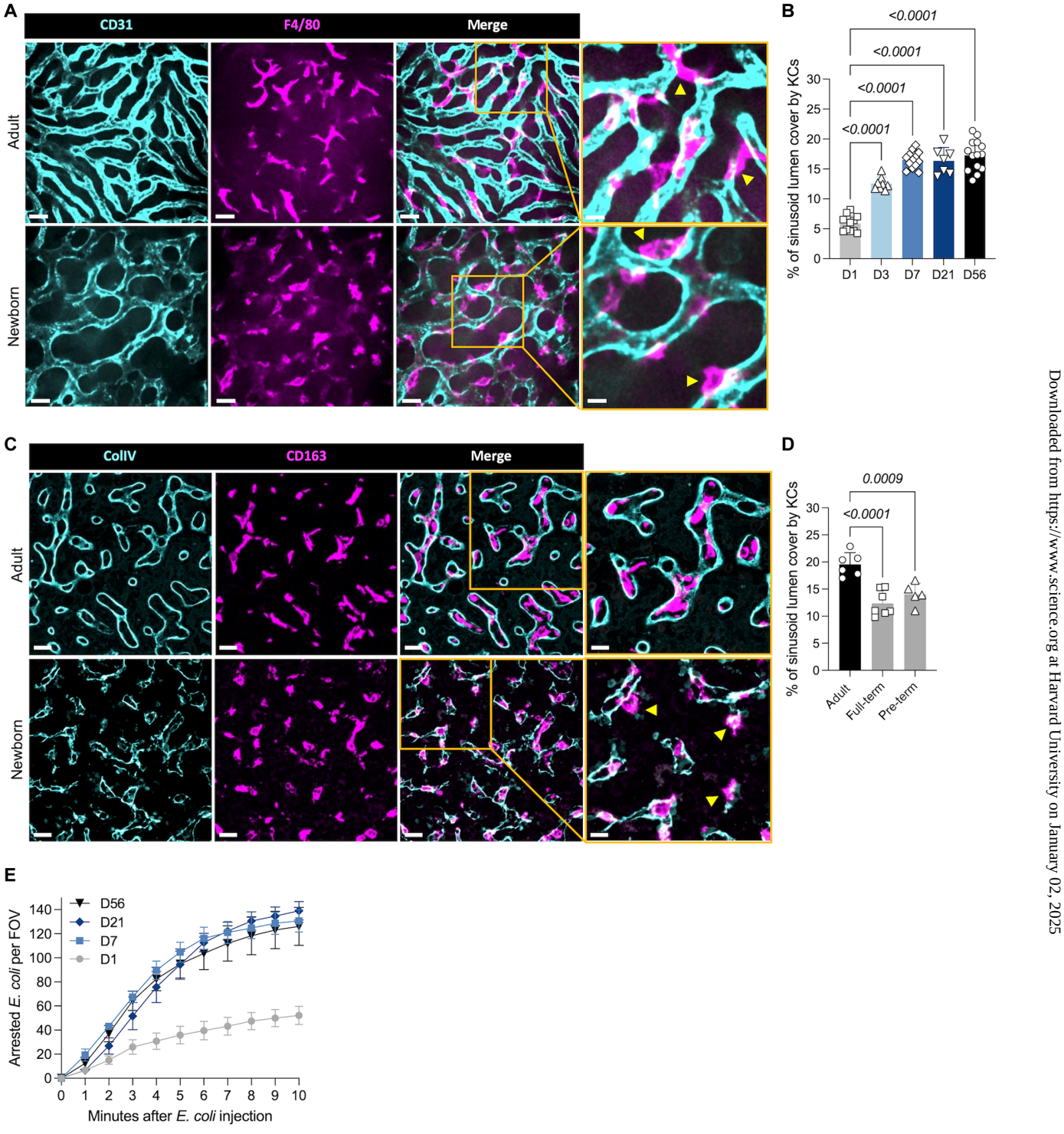

Fig. 3. Adult and newborn KCs adopt distinct locations in the liver. (**A**) Representative IVM of adult and newborn mice showing liver sinusoids labeled with CD31 (cyan) and highlighting KC location (arrowheads) labeled with F4/80 (magenta). Scale bars, 25 and 10 μm. (**B**) Quantification of (A) as liver sinusoidal lumen coverage by KCs at D1, D3, D7, D21, and D56 ($n = 7$ to 14 per group, $N = 4$). (**C**) Representative human liver immunofluorescence showing collagen IV (cyan) and CD163 (magenta). Scale bars, 25 and 10 μm. (**D**) Quantification of (C) as sinusoidal lumen coverage by human CD163–positive cells (macrophages) ($n = 5$ to 7 per group, $N = 2$). (**E**) Time-lapse analysis of *E. coli* arrested in the livers of D1, D7, D21, and D56 mice ($n = 7$ to 9 per group, $N = 4$). Data are presented as individual values with the means ± SD. One-way ANOVA with Dunnett's posttest was used for (B) and (D).

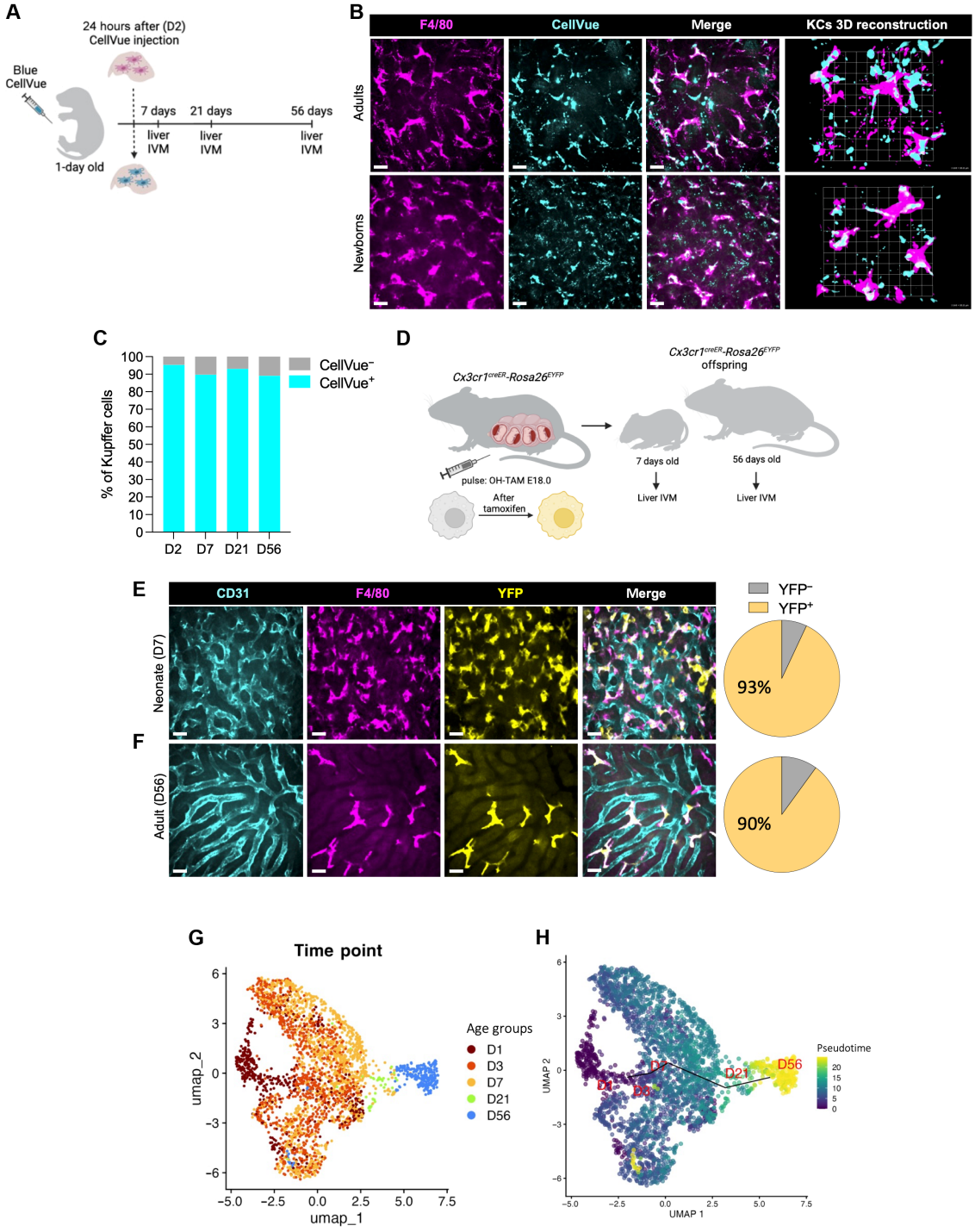

Fig. 4. Newborn KCs relocate to the intravascular compartment within 7 days postpartum. (**A**) CellVue dye injection scheme with newborn injection at D1 and liver intravital performed at D2, D7, D21, and D56. (**B**) Representative IVM of KCs labeled with F4/80 (magenta) with internalized CellVue (cyan) in newborn and adult mice. 3D reconstruction highlights the presence of the dye inside KCs in adult and newborn KCs. Scale bars, 45 μm. (**C**) Quantification of (B) as the frequency of KCs positive for CellVue ($n = 4$ per group, $N = 2$). (**D**) Fate mapping of CX3CR1-expressing cells after 4-OH-tamoxifen injection in Cx3cr1^{creER}-Rosa26^{EYFP} pregnant mice at E18. Liver IVM was performed in the dams at D7 and D56. (**E**) Representative liver IVM of D7 mice with EYFP (yellow) labeling in KCs of Cx3cr1^{creER}-Rosa26^{EYFP} mice induced with 4-OH-tamoxifen (E18). KCs were labeled with F4/80 (magenta), and blood vessels were labeled with CD31 (cyan). Quantification of frequency of EYFP^{+} KCs on the right ($n = 4$, $N = 2$). Scale bars, 45 μm. (**F**) Representative liver IVM of D56 mice with EYFP (yellow) labeling in KCs of Cx3cr1^{creER}-Rosa26^{EYFP} mice induced with 4-OH-tamoxifen (E18). KCs were labeled with F4/80 (magenta), and blood vessels were labeled with CD31 (cyan). Quantification of the frequency of EYFP^{+} KCs on the right ($n = 4$, $N = 2$). Scale bars, 45 μm. (**G**) UMAP of KCs from a liver scRNA-seq database (*28*) of mice at D1, D3, D7, D21, and D56. Dataset colored according to age group. (**H**) UMAP showing lineage trajectory analysis of KCs from D1 to D56. Dataset colored according to a progression in cell differentiation.

reduction with Uniform Manifold Approximation and Projection (UMAP) using a liver scRNA-seq dataset showed that KCs of different ages clustered together in a transition from time point to time point (Fig. 4G), and a trajectory inference analysis showed a linear progression in cell development over time from D1 to D56 (Fig. 4H).

We also investigated whether the KC migration into the liver sinusoids was zone specific, given that it has been recently shown that liver zonation influences hepatic metabolism as well as KC distribution and immune functions (*33*, *34*). Intravital imaging of adult Clec4f reporter mice (*Clec4F*$^{cre\text{-}nTdTomato/+}$/*Rosa26*$^{ZsGreen/+}$) showed that KCs were concentrated in the periportal regions (fig. S4C). This asymmetric distribution is controlled by commensal bacteria in a process that happens around 20 to 25 days postpartum (*33*). At D1 and D7 after birth, Clec4f^{+} cells were homogenously distributed in the liver, suggesting that the KC migration into the sinusoids precedes the KC spatial polarization (fig. S4C).

Relocation to the sinusoids precedes age-associated transcriptional reprogramming in KCs

In contrast with D1 newborn KCs, D7 KCs covered a similar proportion of sinusoidal lumen and efficiently captured *E. coli* in vivo when compared with adult KCs (Fig. 3, B and E). To better understand the differences between KCs at different life stages, we initially profiled newborn (D1), 7-day-old (D7), and adult (D56) KCs using multiparametric flow cytometry. Bona fide KCs were isolated from *Clec4F*$^{cre\text{-}nTdTomato}$ mice and gated on the basis of their expression of F4/80^{high}CD11b^{+}Clec4f^{tdtomato} (fig. S5A). Dimensionality reduction with t-distributed stochastic neighbor embedding (tSNE) showed that D1 and D7 KCs are phenotypically more similar to each other when compared with adult KCs (Fig. 5, A to F, and fig. S5B). Whereas KCs from all three age groups displayed high expression levels of TIM4 (Fig. 5B), D56 KCs had homogenously high levels of CRIg, whereas D1 and D7 KCs showed greater heterogeneity (Fig. 5C and fig. S5C). Major histocompatibility complex class II (MHC-II), which is highly expressed on mature KCs (adult mice; D56), was not yet expressed on KCs from D1 and D7 mice (Fig. 5D and fig. S5C). A similar pattern was found for MHC-II expression in resident macrophages across tissues (fig. S5, D to F), with newborn resident macrophages showing lower expression in comparison with adult counterparts (fig. S5, G to J). Other markers, including MerTK, Clec2, CD11a, and CD29, were also more robustly expressed on adult KCs, whereas CD44 had higher expression patterns in newborns (Fig. 5, E and F, and fig. S5, B and C). By contrast, Fc receptors associated with bacterial recognition and capture, such as CD16 (FcγRIII) and CD64 (FcγRI), were highly expressed by newborn KCs in comparison with adult macrophages (fig. S5C), suggesting that newborn KCs may have greater intrinsic antimicrobial function. This observation was not restricted to KCs but extended to lung alveolar and interstitial macrophages in newborns compared with adults (fig. S5, H and I).

To investigate the differentiation status of KCs at the gene expression level, we used a public scRNA-seq database (*28*) to measure KC core genes and transcription factors (Fig. 5, G and H, and fig. S6A). With *Clec4f* as a reference gene, we identified two main populations among liver cells: KCs and Dcn^{+} macrophages (fig. S6B) (*28*). The KC population was identified on the basis of the combined expression of *Adgre1*, *Timd4*, and *Clec4f*, and the Dcn^{+} macrophage cluster was excluded on the basis of the expression of *Dcn* (fig. S6, B to F). Doublet clusters were subsequentially removed on the basis of the expression of lineage markers (fig. S6, G to J). We did not detect *Epor* and *Klf1* in our KC cluster, excluding a potential contamination with EBI macrophages (fig. S6K) (*20*, *21*). More recently, KCs were shown to be divided into two subpopulations, a major KC1 population and a minor KC2 population (*35*, *36*). We assessed the frequency of KC2 and found it to be lower than 5% at D1, D7, and D56 by flow cytometry; as such, we treated KCs as a single population (fig. S7, A and B). KC core genes *Cd5l*, *Clec4f*, *Vsig4* (encoding CRIg), *Lyz2*, *Csfr1*, and *Folr2* showed high expression at D1, with a small gradual increase as mice aged (Fig. 5G). Other identity markers such as *Timd4*, *Adgre1* (encoding F4/80), *Marco*, *Slc40a1*, and *Msr1* increased over the first 7 days, but then expression levels slightly waned with time (Fig. 5G). *C1pb*, *Hmox1*, and *Vcam1* showed higher expression in newborns (Fig. 5G). *Cd207*, a gene expressed by liver capsule macrophages (*37*), was not expressed at any age. *Ccr2* and *Ms4a3* were not expressed at any age, consistent with the KCs not being monocyte derived, even 8 weeks after birth (Fig. 5G) (*32*). *Kit*, a gene associated with immature cells, also showed negligible expression by KCs at any age (Fig. 5G).

DNA3 and liver X receptor-α (LXRα) are two of the key transcription factors previously described to affect KC identity (*17*, *30*, *38*). *Id3* (encoding DNA3) was the most expressed transcription factor among all age groups (Fig. 5H). Over the first 7 days, *Id3*, *Fos*, and *Spic* showed higher expression when compared with D56 (Fig. 5H). *Nr1h3* (encoding LXRα), *Spic1*, *Id1*, and *Irf7* are up-regulated in embryonic macrophages upon entry into the fetal liver (*17*). In our analysis, *Irf7*, *Maf*, and *Nr1h3* expression levels were increased from D1 to D7 and continued to further increase toward adulthood (D56) (Fig. 5H). Other transcription factors, such as *Hes1*, *Tcf7l2*, *Zfp36l1*, and *Jun*, showed peak expression before adulthood (Fig. 5H). In addition to the expression level, analysis of transcription factor activity showed that *Fos* and *Spic* activity was consistent during the first week, whereas *Hes1*, *Jun*, and *Rxra* activity increased from D1, reaching their peak at D7 and followed by a notable decrease in adults (fig. S7C). *Irf7*, *Maf*, and *Nr1h3* also increased in activity during the first week but remained highly active until adulthood (fig. S7C). To provide a more robust assessment of changes in transcription factors, the top 10 most-predicted differentially active transcription factors were identified in KCs from newborns to adults (fig. S7D). These results suggest that the KC translocation into the vasculature is coupled with up-regulation of some genes associated with the adult KC identity status. In contrast, some genes, including *Fos* and *Spic*, were at peak levels during the first week of life and declined in expression and activity with time (Fig. 5H and fig. S7C). Principal components analysis (PCA) revealed stronger correlation among KCs during the first week of life (D1, D3, and D7) (Fig. 5I) and an overall similar gene expression signature at D1, D7, and D56 after birth, with only 142 differentially expressed (DE) genes when comparing these three age groups (fig. S7E). Pathway enrichment analysis of DE genes showed some differences between D1 and D7 KCs, including a positive regulation of metal and ROS metabolism at D1, whereas at D7, the pathways enriched were toward T cell migration and proliferation (fig. S7, F and G).

From these gene expression data, it is hard to conclude whether KCs at D1 had reduced intrinsic capacity to capture bacteria when compared with D7 or D56. To test this, adult and newborn KCs (F4/80^{+}TIM4^{+}) were isolated and incubated in vitro with opsonized *E. coli* (Fig. 5J). Adult and newborn KCs placed in the same in vitro environment with equal exposure to bacteria showed that both groups efficiently internalized *E. coli*, with newborn KCs being even

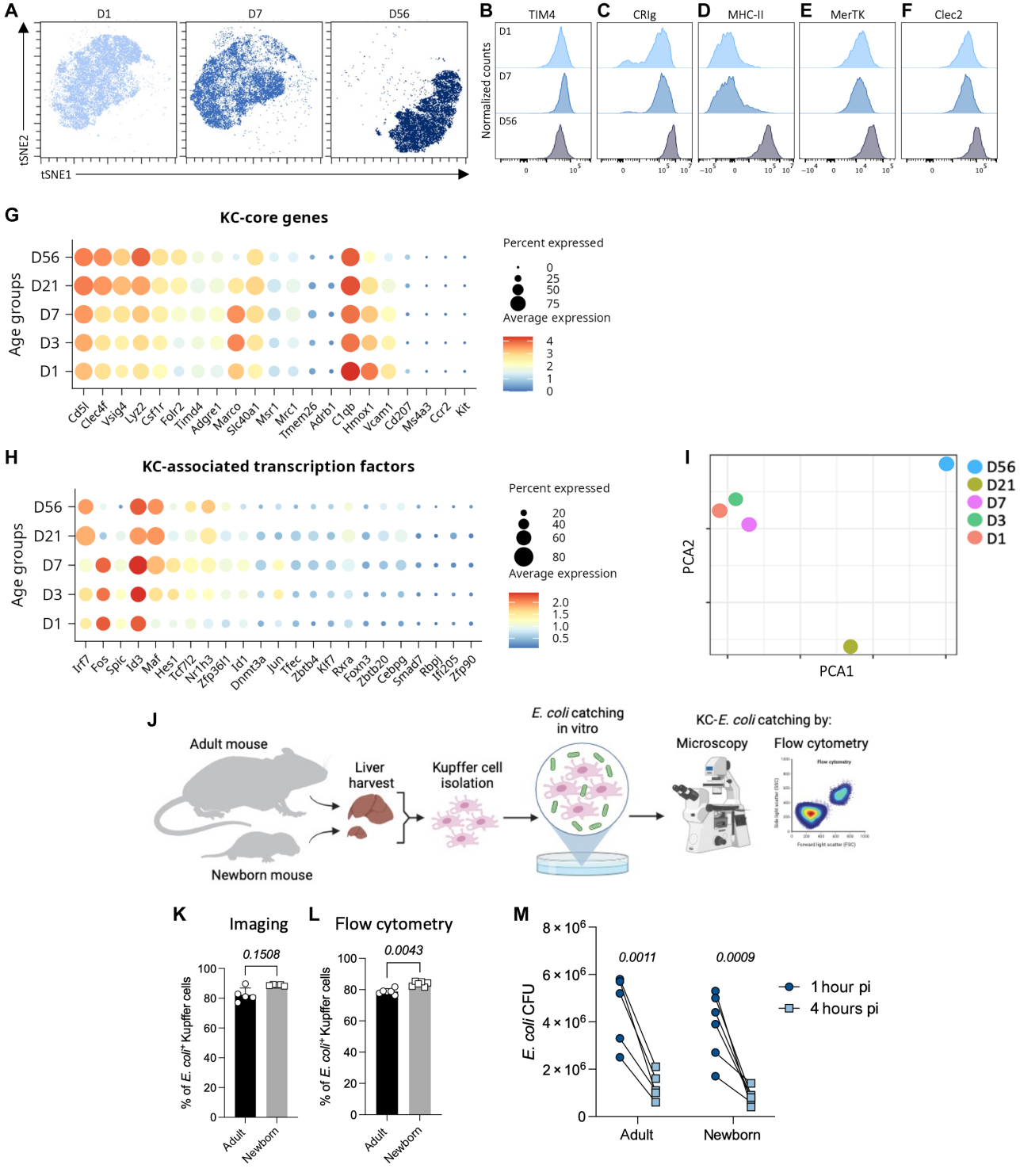

Fig. 5. Relocation to the sinusoids precedes age-associated transcriptional reprogramming in KCs. (**A**) t-SNE showing adult (D56), neonate (D7), and newborn (D1) KCs. KCs were pregated as shown in fig. S5A. (**B** to **F**) Representative histogram overlay of (B) TIM4, (C) CRIg, (D) MHC-II, (E) MerTK, and (F) Clec2 expression by D1, D7, and D56 KCs, gated as shown in fig. S5A. (**G**) Dot plot of liver scRNA-seq showing expression of KC-core genes in D1, D3, D7, D21, and D56 mice. (**H**) Dot plot of liver scRNA-seq showing expression of KC-associated transcription factors in D1, D3, D7, D21, and D56 mice. (**I**) Principal components analysis of KCs in D1, D3, D7, D21, and D56 mice. (**J**) Experimental design for *E. coli*–catching and –killing in vitro assay. (**K**) Frequency of adult and newborn KCs ($F480^{+}TIM4^{+}$) isolated and infected in vitro by confocal imaging ($n = 5$ per group, $N = 2$). (**L**) Frequency of adult and newborn KCs ($F480^{+}TIM4^{+}$) isolated and infected in vitro by flow cytometry ($n = 6$ per group, $N = 2$). (**M**) Bacterial burden of KCs 1 and 4 hours after *E. coli* infection in vitro ($n = 5$ or 6 per group, $N = 2$). Data are presented as individual values with the means ± SD. Mann-Whitney test was used for (K) and (L). RM two-way ANOVA with Šidák's multiple comparison posttest was used for (M).

more efficient than adult KCs (Fig. 5, K and L). To examine potential effects of the KC isolation process, we systematically assessed expression of F4/80, TIM4, and CRIg. After isolation and incubation, these proteins did not change and were at levels similar to those seen in vivo (fig. S8, A to G). Associated with catching ability, newborn KCs were also efficient in killing *E. coli* in vitro when compared with adult KCs (Fig. 5M). These results indicate that newborn KCs are capable of capturing and killing *E. coli* when in direct contact with the bacteria.

CD74/MIF and CD44 control KC migration into the sinusoids

Exposure to commensals at birth could be a potential strong stimulus for initiating/priming the translocation of KCs into the sinusoids. To test this hypothesis, we performed liver intravital imaging in germ-free (GF) D7 mice, which revealed no delay in KC translocation from the parenchyma to the sinusoidal lumen and essentially identical KC numbers regardless of the microbiome status (Fig. 6A and fig. S9A). To further investigate a potential role of the microbiota in KC translocation, GF dams were colonized with a wild microbiome harvested from wild mice, which have been shown to be more similar to humans and to better predict human disease responses (*39*, *40*). Rewilded pups showed no expedited translocation of KCs into the sinusoids (Fig. 6A and fig. S9A). Furthermore, the KC number and coverage of the sinusoidal lumen remained nearly identical among specific pathogen–free (SPF), GF, and rewilded mice at D21 (fig. S9, B and C). In our scRNA-seq dataset analysis, the scavenger receptor *Marco* was highly expressed in newborns, with a significant increase over the first week of life (Fig. 5F). Another scavenger receptor, *Msr1*, had lower but consistent expression over the first few days of life (Fig. 5F). However, mice deficient in both MARCO and MSR-1 showed no effect on the relocation of KCs into the sinusoids, suggesting a limited role for these molecules (Fig. 6B).

We next focused on other molecules that might induce the migration of KCs into sinusoids. Because it has been shown that CXCR3 is important in KC distribution and immune zonation (*33*), we first examined CXCR3$^{-/-}$ mice, and no significant difference was observed in KC relocation into the sinusoids during the first week of life (Fig. 6C). Among the classical chemokine receptors, only CCR5 was upregulated over the first 7 days of life. However, CCR5$^{-/-}$ mice had only a minor delay in KC translocation into the sinusoids (Fig. 6C). KC number was similar between WT, MARCO$^{-/-}$MSR-1$^{-/-}$, CXCR3$^{-/-}$, and CCR5$^{-/-}$ mice (fig. S9D).

We next compared the gene expression profiles of D1 versus D7 KCs to identify other potential molecules regulating KC migration. *Cd74* and *Cd44* were among the top DE genes (Fig. 6D), with substantial enrichment of *Cd44* at D7, and *Cd74* continued to be the top DE gene to adulthood (D56) (Fig. 6E). CD74 is an MHC-II–associated protein invariant chain that has been associated with dendritic cell migration (*41*), whereas CD44 is a cell-surface glycoprotein reported to be involved in cell adhesion and migration, particularly in liver sinusoids (*42*). The ligand for CD74 has been reported to be macrophage migration inhibitory factor (MIF) (*43*), a cytokine expressed by multiple tissues and cell types that induces macrophage migration. In the liver, a variety of cells showed *Mif* expression (Fig. 6F). In addition, the level of MIF in the circulation was highest in newborns (D1) and strongly decreased once KCs assumed their final location (Fig. 6G).

To test the potential role of CD74/MIF and CD44 in KC translocation, liver intravital imaging was performed in D7 CD74$^{-/-}$ mice, CD44$^{-/-}$ mice, and mice treated with an MIF antagonist (Fig. 6H) (*44*). CD74$^{-/-}$ mice displayed a delay in KC relocation into the sinusoids (Fig. 6I). CD44 deletion and inhibition of MIF led to an extended delay in KC relocation, with ~50% impairment in luminal coverage of sinusoids (Fig. 6I). Whereas MIF binds other receptors besides CD74, including CXCR4, CXCR2, and Ackr3 (CXCR7) (*45*, *46*), none of these receptors were found on KCs (fig. S9, E to H). Because deletion of these molecules could also affect the migration of hematopoietic stem cells to fetal liver, we also quantified the number of KCs by imaging and flow cytometry. None of these strains or mice treated with the MIF antagonist had reduced KC numbers in the liver, suggesting that specifically translocation into the lumen of the sinusoids was impaired in CD74$^{-/-}$ mice, MIF antagonist–treated mice, and CD44$^{-/-}$ mice (Fig. 6, J to L). Morphologically, all groups showed KCs with similar volumes, whereas CD74$^{-/-}$, MIF antagonist–treated, and CD44$^{-/-}$ mice presented more elongated and polarized KCs in comparison with controls (fig. S9, I to K). Last, in older mice, only CD44$^{-/-}$ mice showed a significant delay in sinusoidal coverage at D21 despite similar cell numbers (fig. S9, L and M), a phenotype not seen at D56.

Delay in KC translocation correlates with increased bacterial dissemination

Given our finding that naïve mice showed a similar *E. coli*–catching ability in the liver at day 7 after birth compared with adults, we next tested whether a delay in KC translocation would also affect bacterial capture and dissemination. CD74$^{-/-}$, MIF antagonist–treated, and CD44$^{-/-}$ mice were infected with *E. coli*. Intravital microscopy revealed a notable reduction in bacteria arrested in the livers of these groups when compared with control counterparts (Fig. 7, A and B). The frequency of *E. coli*$^{+}$ KCs was significantly reduced in CD74$^{-/-}$, CD44$^{-/-}$, and MIF antagonist–treated mice by intravital microscopy (Fig. 7C). In MIF antagonist–treated and CD44$^{-/-}$ mice, more than 50% of KCs and 43% of KCs in CD74$^{-/-}$ mice were unable to capture any bacteria versus only 30% in WT mice (Fig. 7, D to G). In KCs that caught bacteria, most had only one *E. coli* captured (Fig. 7, D to G).

To better understand how the absence of CD74 and CD44 as well as how MIF antagonist treatment affect KCs, we analyzed expression of surface proteins in KCs from D7 mice using flow cytometry (fig. S10, A to N). In CD74$^{-/-}$ mice, we observed lower expression levels of ESAM, CD206, MerTK, and CD32 (fig. S10, A to N). Similarly, MIF antagonist treatment led to reduced levels of ESAM, CD206, MerTK, and CD32, with a subtle increase in the mean expression of TIM4, CRIg, CD11a, and CD64 (fig. S10, A to N). CD44$^{-/-}$ KCs exhibited a modest increase in MerTK, CD64, and CD32, with no significant changes in the other markers (fig. S10, A to N). Overall, the subtle differences in protein expression found in CD74$^{-/-}$, MIF antagonist–treated, and CD44$^{-/-}$ mice were unlikely to explain the impaired catching of *E. coli* in vivo. These different knockout mice also had very minor differences in expression profiles when examining other tissue-resident macrophages (fig. S10, O to R). Because interfering with CD74, CD44, and MIF signaling could have effects beyond the neonatal phase, we also examined positioning of KCs and bacterial catching and dissemination in adult mice. The number of KCs and the lumen coverage were similar when comparing CD74$^{-/-}$, CD44$^{-/-}$, and MIF antagonist–treated mice with their control counterparts (fig. S11, A and B). Liver and blood bacterial burdens were similar among the adult groups, suggesting that neither CD74/MIF nor CD44 have any notable effects after KCs enter the sinusoids (fig. S11, C and D).

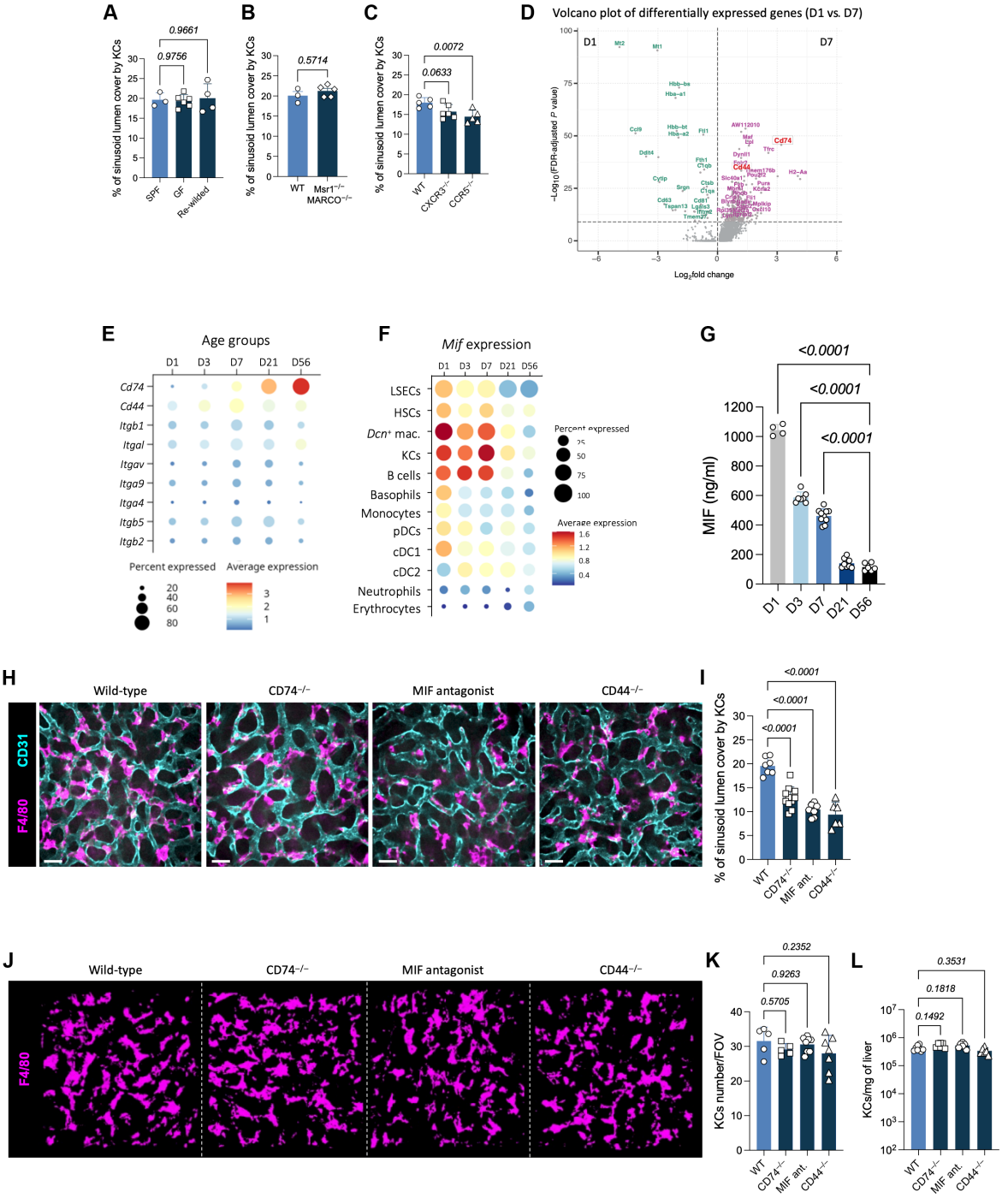

Fig. 6. CD74/MIF and CD44 control KC migration into the sinusoids. (**A**) IVM quantification of sinusoidal lumen coverage by KCs in SPF, GF, and rewilded D7 mice ($n = 3$ to 6 per group, $N = 2$). (**B**) IVM quantification of sinusoidal lumen coverage by KCs in WT and Msr1$^{-/-}$/MARCO$^{-/-}$ D7 mice ($n = 3$ to 5 per group, $N = 2$). (**C**) IVM quantification of sinusoidal lumen coverage by KCs in WT, CXCR3$^{-/-}$, and CCR5$^{-/-}$ D7 mice ($n = 5$ or 6 per group, $N = 2$). (**D**) Volcano plot showing the top 15 DE genes between KCs in D1 and D7 mice highlighting the up-regulation of *Cd74* and *Cd44* at D7. (**E**) Dot plot of liver scRNA-seq showing expression of *Cd74*, *Cd44*, and integrins by KCs in D1, D3, D7, D21, and D56 mice. (**F**) Dot plot of liver scRNA-seq showing *Mif* gene expression by different liver cells in D1, D3, D7, D21, and D56 mice. (**G**) MIF serum concentration in D1, D3, D7, D21, and D56 mice ($n = 4$ to 10 per group, $N = 2$). (**H**) Representative liver IVM of WT, CD74$^{-/-}$, MIF antagonist–treated, and CD44$^{-/-}$ D7 mice of KCs labeled with F4/80 (magenta) and sinusoids labeled with CD31 (cyan). Scale bars, 25 μm. (**I**) Quantification of (H) as frequency of sinusoidal lumen coverage by KCs in WT, CD74$^{-/-}$, MIF antagonist–treated, and CD44$^{-/-}$ D7 mice ($n = 6$ to 11 per group, $N = 4$). (**J**) 3D reconstruction of KCs labeled with F4/80 (magenta) in WT, CD74$^{-/-}$, MIF antagonist–treated, and CD44$^{-/-}$ D7 mice. Scale bars, 25 μm. (**K**) Quantification of (J) as KC number per FOV in WT, CD74$^{-/-}$, MIF antagonist–treated, and CD44$^{-/-}$ D7 mice ($n = 5$ to 8 per group, $N = 2$). (**L**) KC number per milligram of liver by flow cytometry in WT, CD74$^{-/-}$, MIF antagonist–treated, and CD44$^{-/-}$ D7 mice ($n = 6$ to 8 per group, $N = 2$). Data are presented as individual values with the means ± SD. Mann-Whitney test was used for (B). One-way ANOVA with Dunnett's posttest was used for (A), (C), (G), (I), (K), and (L).

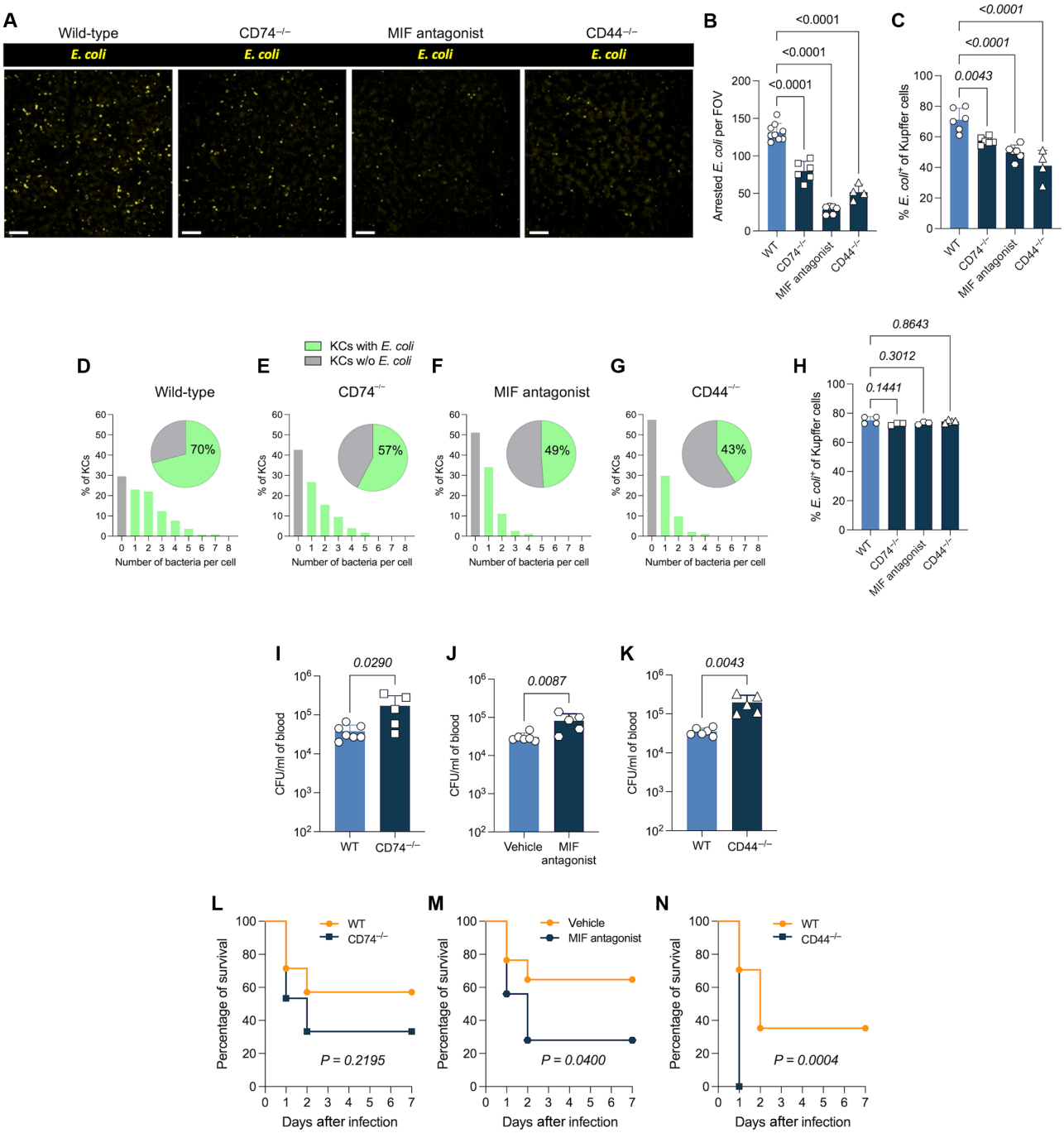

Fig. 7. Delayed KC migration increases *E. coli* systemic dissemination. (**A**) Representative liver IVM of WT, CD74$^{-/-}$, MIF antagonist–treated, and CD44$^{-/-}$ D7 mice 30 min after *E. coli* (yellow) challenge. Scale bars, 50 μm. (**B**) Quantification of (A) as number of *E. coli* arrested in the liver per FOV ($n = 4$ to 9 per group, $N = 3$). (**C**) Frequency of infected KCs by IVM in WT, CD74$^{-/-}$, MIF antagonist–treated, and CD44$^{-/-}$ D7 mice ($n = 4$ to 6 per group, $N = 2$). (**D** to **G**) Frequency of KCs with internalized *E. coli* (pie chart) and number of bacteria per individual cell in WT, CD74$^{-/-}$, MIF antagonist–treated mice, and CD44$^{-/-}$ mice (bar graph) ($n = 4$ to 6 per group, $N = 2$). (**H**) Frequency of WT, CD74$^{-/-}$, MIF antagonist–treated, and CD44$^{-/-}$ KCs (F480^{+}TIM4^{+}) isolated from D7 mice and infected in vitro by confocal imaging ($n = 3$ or 4 per group, $N = 2$). (**I**) WT and CD74$^{-/-}$ D7 mice were infected with 1×10^8 CFU *E. coli* Xen14 (normalized per 20 g of body weight), and bacterial loads were determined 30 min after infection ($n = 5$ or 6 per group, $N = 2$). (**J**) WT and MIF antagonist–treated D7 mice were infected with 1×10^8 CFU *E. coli* Xen14 (normalized per 20 g of body weight), and bacterial loads were determined 30 min after infection ($n = 5$ or 6 per group, $N = 2$). (**K**) WT and CD44$^{-/-}$ D7 mice were infected with 1×10^8 CFU *E. coli* Xen14 (normalized per 20 g of body weight), and bacterial loads were determined 30 min after infection ($n = 5$ or 6 per group, $N = 2$). (**L** to **N**) Survival of WT, CD74$^{-/-}$, MIF antagonist–treated, and CD44$^{-/-}$ D7 mice infected with 5×10^7 CFUs *E. coli* Xen14 (normalized per 20 g of body weight) ($n = 10$ to 25 per group, $N = 3$). Data are presented as individual values with the means ± SD. One-way ANOVA with Dunnett's posttest was used for (B), (C), and (H). Mann-Whitney test was used for (I), (J), and (K). Kaplan-Meier test with Gehan-Breslow-Wilcoxon curve comparison was used in (L), (M), and (N).

To determine whether CD44 was associating with its ligand, hyaluronan, mice were treated intraperitoneally daily for the first 7 days of life with hyaluronidase (fig. S11E). Hyaluronidase treatment effectively reduced ~70% of hyaluronan in the liver vasculature, leading to a mild delay in KC translocation without affecting the cell number (fig. S11, F to I). These data are consistent with the CD44-hyaluronan pathway being a key adhesion pathway in liver sinusoids in newborns, much like in adults (*42*).

Given that integrins are known to have a large impact on both the development and the trafficking of immune cells and that the downstream signaling of CD74/MIF has been associated with an increase in β1-integrin expression (*47*), we examined the role of integrins in the translocation of KCs into the sinusoids. *Itgb1* (encoding CD29) was detected at all ages (Fig. 6E), with a progressive increase during the first week of life, similar to what we observed for *Cd74* and *Cd44*. Other integrins such as *Itgal* (encoding CD11a) followed a similar pattern as *Itgb1*, and numerous other integrins had some basal integrin expression (Fig. 6E). Blockade of β1 and β2 integrin during the first week of life resulted in a 20 to 30% reduction in KC relocation, with no alteration in KC numbers (fig. S11, J to L). The delay in KC migration mediated by β-integrin blocking decreased *E. coli* capture in the liver (fig. S11, M to O), albeit to a lesser extent than CD44 and MIF antagonist treatment. Moreover, integrin inhibition also resulted in KCs with smaller and more spherical morphology (fig. S11, P to R), as previously reported (*48*). As such, the integrins may contribute to some extent to the translocation of KCs but do not mediate all of the migration.

To determine whether CD74 and CD44 deletion, as well as MIF antagonist treatment, had effects on KCs beyond affecting translocation into sinusoids, KCs were isolated from WT, $CD74^{-/-}$, $CD44^{-/-}$, and MIF antagonist–treated D7 mice, and the cells were incubated in vitro with bacteria (Fig. 7H). KCs from all groups internalized bacteria to the same degree, suggesting that their intrinsic capacity to capture bacteria was not altered by CD44 or CD74 deficiency or MIF inhibition (Fig. 7H). As a consequence of the reduced ability to capture bacteria in vivo by KCs, $CD74^{-/-}$, MIF antagonist–treated, and $CD44^{-/-}$ D7 mice showed significantly higher bacterial burden in the blood 30 min after infection (Fig. 7, I to K). Moreover, the bloodstream infection was associated with proportionally higher mortality rates in these groups (Fig. 7, L to N).

DISCUSSION

Here, we report that newborn susceptibility to bacterial infection is directly related to the limited bloodstream access of KCs at birth and that these cells undergo a fundamental change in location within the first week of life. We show that right after birth, KCs require reverse transmigration from the liver parenchyma into the sinusoids, where they provide the critical function of sterilizing blood of any pathogens. Whereas intravital imaging could not be performed on live human samples, results from human tissue sections support our findings in mice. This relocalization was not induced by the introduction of a commensal microbiome and appears to be an autonomous pathway that requires the adhesion molecule CD44 and an enigmatic cytokine MIF that binds CD74. MIF has been shown to be produced by endothelial and epithelial cells (*49*) as well as megakaryocytes and other cells to induce chemotaxis via CD74 (*50*). Our data are consistent with MIF potentially acting as a chemoattractant for neonatal KCs. However, the MIF receptor CD74 lacks obvious signaling properties and is therefore unlikely to function as a canonical chemokine receptor. Coincidently, CD44 has been reported to be a component of the MIF-CD74 complex, working as a co-receptor needed for downstream signaling (*43*), and we observed the same molecules being critical for the reverse transmigration of KCs from parenchyma into the liver sinusoids. Therefore, in addition to its adhesion properties, CD44 may contribute to the MIF signaling that leads to KC reverse transmigration at birth.

Studies showing the presence of KCs at birth often assumed their location to be the same as that in adults (*16*, *18*, *51*), which highlights an important gap in the knowledge of KCs during the transition from fetal to postnatal life. Our data suggest that a population of progenitor macrophages remains in the fetal liver parenchyma, where they activate various liver-specific transcription pathways and take on many of the characteristics of liver KCs but still need to relocate to the sinusoidal lumen to perform their functions. Given that there were numerous KC transcriptional changes over the first 7 days, it is plausible that, in addition to translocation into sinusoids, up-regulation of an antimicrobial molecule could also contribute to better clearance of *E. coli*. That KCs from newborns eradicated *E. coli* in vitro does suggest that KCs from newborns have significant antimicrobial capabilities. We previously observed that natural antibodies including IgM and IgG3 enhanced the catching ability of *E. coli* by KCs in female mice, but this was in older mice where KCs already had unrestricted contact with blood. That none of these opsonins could improve catching of *E. coli* in newborns further supports the observation that newborn KCs simply cannot access the bacteria in the bloodstream regardless of their opsonin status. Our finding that KCs in newborns were located on the parenchymal side of the vasculature could potentially explain the very significant susceptibility of neonates to bloodstream infections. Subsequently, once KCs migrate into the sinusoids, opsonins could become important and lead to a strong decrease in mortality from blood stream infections.

Neonatal sepsis and meningitis remain a huge problem, and there remains an unmet clinical need particularly for *E. coli*–induced infections. Our data suggest that at birth, the main filter for *E. coli*, the KC, has not yet relocated to the sinusoidal lumen where it can clear this infection. This would extend to premature infants, who likely would have an even increased deficit in this filtering process. Elucidating the molecular mechanisms that underlie the translocation of KCs into the sinusoids in newborns could open innovative treatment modalities. For example, one could potentially increase CD44 and CD74 expression in KCs at birth combined with the development of MIF agonists that could function to coax KCs into the sinusoids for better eradication of circulating pathogens and prevention of *E. coli*–induced sepsis and meningitis.

MATERIALS AND METHODS

Study design

This study aimed to elucidate the role of KCs in newborn susceptibility to bacterial infections and to characterize KC dynamics early in life. Newborn (1-day-old) and adult (8-week-old) C57BL/6 mice were intravenously challenged with *E. coli*. Liver intravital microscopy was used to evaluate the in vivo bacterial capture capabilities of KCs and to characterize their number, distribution, morphology, and location. The imaging revealed a marked reduction in sinusoidal lumen coverage by KCs in newborn mice compared with adults. To

further investigate the developmental changes in KC function, additional experiments were conducted with mice at 3, 7, and 21 days old. By 7 days after birth, KC distribution and bacterial capture capabilities approached those observed in adult mice. Flow cytometry and gene expression profiling were used to explore KC changes during the first week of life. KC migration mechanisms were investigated using various mouse strains and treatment conditions. Sample sizes were generally informed by prior studies and internal laboratory benchmarks, with a minimum of three animals per group used when novel approaches were used. Human liver samples were analyzed for comparative liver macrophage characteristics, with sample sizes determined on the basis of tissue availability and preservation status. Data were not excluded, and all experiments were replicated at least once with consistent results. Randomization was used for pharmacological treatments and infection conditions; however, blinding was implemented after data collection for imaging analysis, given that images were assigned random keys and processed using the same workflow.

In vivo animal studies

Experiments were carried out using 1-, 7-, and 56-day-old mice unless otherwise stated. All mice were used in a C57Bl/6 background, and a mix of male and female mice were used for each experiment. The experimental procedures were approved by the University of Calgary Animal Care Committee and were in accordance with Canadian Council for Animal Care Guidelines (Protocol No. AC19-0138; AC21-0211). GF mice were bred and housed at the International Microbiome Centre, University of Calgary, Canada. Rewilded mice were obtained from GF mice previously colonized with a wild microbiome and cohoused and bred in isolators at the Wild Microbiome and Immunity facility, University of Calgary, Canada. Other mice were cohoused and bred in an SPF facility at the University of Calgary with a 12-hour light/dark cycle and access to food and water ad libitum. C56BL/6 mice (WT) were obtained from the Jackson Laboratory and subsequently bred in house. Cxcr3$^{-/-}$ (B6.129P2-Cxcr3^{tm1Dgen}/J), Msr1$^{-/-}$ (B6.Cg-*Msr1*^{tm1Csk}/J), Ccr5$^{-/-}$ (B6.129P2-*Ccr5*^{tm1Kuz}/J), Cd44$^{-/-}$ (B6.129(Cg)-*Cd44*^{tm1Hbg}/J), Cx3cr1-cre^{ER} (B6.129P2(Cg)-*Cx3cr1*$^{tm2.1(cre/ERT2)Litt}$/WganJ), Ai14 (B6.Cg-Gt(ROSA) *26Sor*$^{tm14(CAG-tdTomato)Hze}$/J), and Ai6 (B6.Cg-*Gt(ROSA)26Sor*$^{tm6(CAG-ZsGreen1)Hze}$/J) mice were obtained from the Jackson Laboratory and subsequently bred in house. Marco$^{-/-}$ mice were a gift from D. Bowdish (McMaster University, Ontario). Msr1$^{-/-}$ and Marco$^{-/-}$ mice were bred in house to generate the Msr1$^{-/-}$/Marco$^{-/-}$ double knockout. Cd74$^{-/-}$ mice were a gift from I. Shachar (Weismann Institute of Science, Israel). Clec4F-cre^{nTdTomato} mice were a gift from C. Glass (University of California, San Diego). Clec4F-cre^{nTdTomato} mice were crossed with Ai6 (B6.Cg-*Gt(ROSA)26Sor*$^{tm6(CAG-ZsGreen1)Hze}$/J) mice. Ms4a3-cre mice were a gift from F. Ginhoux (A*STAR, Singapore). Both Ms4a3-cre and Cx3cr1-cre^{ER} mice were crossed with Ai14 (B6.Cg-Gt(ROSA) *26Sor*$^{tm14(CAG-tdTomato)Hze}$/J) mice.

Human liver tissue samples

Archived formalin-fixed paraffin-embedded (FFPE) liver tissue from perinatal and fetal autopsies was retrieved from the archives of Alberta Precision Laboratory, Calgary, Alberta, Canada. Pediatric tissue was obtained from pregnancy terminations and neonatal and pediatric deaths (see table S1). Cases were grouped into preterm newborns (22 to 30 gestation weeks; $n = 5$) and full-term newborns (31 to 38 gestation weeks; $n = 7$). Autopsy consent was obtained in all cases, and ethics approval was sought for use of surplus diagnostic tissue. FFPE adult liver tissue was obtained from surgical resections ($n = 6$) from Alberta Precision Laboratory, Calgary, Alberta, Canada, and Charite University Medicine, Berlin, Germany. All relevant ethical regulations were followed in this study, and the study was approved by the Conjoint Health Research Ethics Board, University of Calgary (ethic ID REB14-2296), and the Ethics Committee at Charite University Medicine Berlin (Project EA2/091/19).

Bacterial preparation and infection

E. coli strain Xen14, a strain derived from enteropathogenic *E. coli* WS2572, was obtained from PerkinElmer and transformed with pGFP_GM_FRT to constrictively express GFP. This plasmid was a gift from W. Elhenawy (University of Alberta, Calgary). GFP *E. coli* was grown in lysogeny broth (LB) medium at 37°C on a shaker overnight and then subcultured until the logarithmic phase [optimal density at 600 nm (OD_{660}) = 1.0]. Kanamycin was used for culture at a concentration of 30 μg/ml. For infections, a bacterial dose of 1×10^8 CFUs was normalized per 20 g of body weight and injected intravenously, unless otherwise noted. For survival studies, a neonatal mouse sepsis score system was adapted from prior work (*52*) and introduced to monitor newborn mice on the basis of their appearance, activity, response to stimuli, respiration rate, and body temperature. A ranked score from 0 to 5 was created, and scores equal or lower than 1 were considered a humane end point. For evaluation of tissue bacterial burden, organs were harvested, weighed, and homogenized in 1 ml of sterile PBS. The tissue suspension was plated onto kanamycin-containing LB plates in serial dilutions. The CFUs were counted 16 to 20 hours after incubation at 37°C. For bacterial opsonization, 1×10^8 CFUs of *E. coli* was incubated with a 50% serum solution (200 μl of sterile saline + 200 μl of fresh adult female serum) for 15 min at room temperature, washed twice with sterile saline, and resuspended for infection as described above. *S. aureus* strain MW2 was obtained from the Network on Antimicrobial Resistance in *S. aureus* and transformed with pCM29 (*53*) to constitutively express GFP (*54*). Bacteria were cultured overnight under agitation at 37°C in brain heart infusion medium (Difco) with chloramphenicol (10 μg/ml). Before infection, bacteria were subcultured without antibiotics in brain heart infusion medium for 1.5 to 2 hours until exponential phase growth was achieved (OD_{660} nm = 1.0), washed with saline, and resuspended in saline. For imaging infection, a bacteria dose of 1×10^8 CFUs was normalized per 20 g of body weight and injected intravenously. Given the higher virulence of MRSA in comparison with *E. coli* and previous data from our laboratory using adult mice, for survival infection, a bacterial dose of 5×10^6 CFUs normalized per 20 g of body weight was used.

Mouse treatments

The CellVue Claret Far Red Fluorescent Cell Linker Kit (Sigma-Aldrich) was used for the long-term labeling of KCs and prepared according to the manufacturer's instructions. A dose of 10 μM was injected intravenously into newborn mice (1 day old) to label KCs. For genetic cell labeling, we used the tamoxifen-inducible CX3CR1-^{creER}/Rosa26^{tdTomato} mice. 4-Hydroxytamoxifen (Sigma-Aldrich) was reconstituted in ethanol to a concentration of 100 mg/ml, and aliquots were stored at −20°C protected from light. For treatment, the stock solution was diluted in corn oil and administered in a single dose (75 μg/g body weight) into pregnant females at E18.0 via oral gavage (*17*). MIF antagonist (Sigma-Aldrich; catalog 475846) was reconstituted with dimethyl sulfoxide to a concentration of 50 mg/

ml, and aliquots were stored at −20°C protected from light. For treatment, stock aliquots were diluted in corn oil to a final concentration of 1 mg/ml (1 μg/μl) and injected intraperitoneally [5 μg/g; 5 mg/kg (*44*)] at 1, 3, and 5 days old. Intravital imaging and flow cytometry were performed at 7 days old. CD29 and CD18 blocking antibodies (BioXCell; BE0232 and BE0009, respectively) were administered intraperitoneally daily (from day 1 to day 7) at 5 μg/g of body weight, and rat IgG2a was used as an isotype control as recommended. Lyve-1 blocking antibody (R&D Systems; mAb2125) (*55*) was administered intraperitoneally daily (from day 1 to day 7) at 5 μg/g of body weight, and rat IgG2a was used as an isotype control. Hyaluronidase (Sigma-Aldrich; H3506) was administered intraperitoneally daily (from day 1 to day 7) at 20 U/g of body weight, and PBS injection was used as a control.

Preparation for intravital microscopy

Multichannel spinning-disk confocal microscopy was used to image the liver as previously described (*56*). Mice were anesthetized by an intraperitoneal injection of ketamine (200 mg/kg body weight; Bayer Animal Health) and xylazine (10 mg/kg body weight; Bimeda-MTC). Fluorescent-conjugated antibodies were injected intravenously before surgery. Surgery and preparation for liver intravital imaging was done as previously described (*56*). Bacteria were injected intravenously after mice were positioned at the microscope. For newborn brain imaging, the mice were anesthetized as previously described and received the conjugated antibodies intravenously. Next, a skull window was opened with a microscissor, and the mouse was carefully positioned on a heating stage for imaging.

Intravital microscopy

Image acquisition was done using an inverted spinning-disk confocal microscope (IX81; Olympus) equipped with a focus drive by Olympus and a motorized stage (Applied Scientific Instrumentation) to allow live movement on the *x* and *y* axes. The microscope was fitted with a motorized objective turret equipped with 4×/0.16 UPLANSAPO, 10×/0.40 UPLANSAPO, and 20×/0.70 UPLANSAPO objective lenses. The microscope was linked to a confocal light path (WaveFx; Quorum Technologies) based on a modified CSU-10 head (Yokogawa Electric Corporation). Cells of interest were visualized using fluorescent conjugated antibodies, reporter mice, and/or fluorescent bacteria. Laser excitation wavelengths were 491, 561, 642, and 730 nm, and a 512 pixel–by–512 pixel back-thinned EMCCD camera was used for detection. Volocity software (Quorum) was used to drive the confocal microscope and for acquisition and analysis of images. Brain imaging was performed using the same microscope.

Immunohistochemistry of human liver tissue

FFPE liver samples were cut 2-μm thick and sequentially stained as previously described (*57*, *58*). After deparaffinization, heat-mediated Ag retrieval was performed in EDTA (pH 8.0) buffer. Nonspecific fluorescence was eliminated and nonspecific binding blocked before primary antibody incubation. Tissues were then washed and incubated with secondary antibodies, followed by nucleus staining with 4′,6-diamidino-2-phenylindole (DAPI). Sections were imaged for the first markers, and the antibodies were eluted using a 2-mercaptoethanol/SDS buffer initiating a new staining cycle. At the end, tissues were stained for IBA1, CD163, CD16, HepPar1, Coll-IV, and DAPI. Single-field images were acquired on a Zeiss Observer.Z1 microscope (Carl Zeiss, Oberkochen, Germany). Whole-slide scanning was performed on a Zeiss Axio Observer 7.

Single-cell analysis

Murine hepatic scRNA-seq data were downloaded (GSE171993) (*28*). Postnatal D1, D3, and D7 ($n = 4$ each) and D21 and D56 ($n = 2$ each) liver cells were isolated with a two-step perfusion method. RNA-seq libraries were prepared from the isolated cells using the Chromium Single Cell 3′ Kit (V2 chemistry, 10X Genomics). The sequencing was performed on an Illumina HiSeq 4000 at IGM Genomics Center, UCSD. Sample processing to sequencing and all of the preprocessing of sequencing reads, i.e., aligning the reads to mouse reference genome GRCm38, batch effect correction, sequencing depth normalization, and generating an expression matrix, were done by Liang *et al.* (*28*). The more detailed analysis done for this paper can be found in Supplementary Methods.

Macrophage isolation and flow cytometry

Liver nonparenchymal cells were isolated by adapting a protocol previously described (*59*). In brief, mice were anesthetized, and blood was collected for serum analysis. The liver was subsequently removed, chopped finely, and digested in 10 ml of Hanks' balanced salt solution (HBSS) containing collagenase type IV (1 mg/ml; Sigma-Aldrich, C4-28) and deoxyribonuclease I (DNAse I, 30 μg/ml) at 37°C for 30 min on a shaker. After incubation, the suspension was passed through a 100-μm cell strainer and centrifuged at 25*g* for 5 min at room temperature to pellet debris and hepatocytes. The supernatant was transferred to a new tube and centrifuged at 400*g* for 10 min at 4°C to pellet the cells in suspension. The pellet was resuspended in 8 ml of 17% iodixanol solution (Optiprep Density Gradient Meduim), and 1.5 ml of red HBSS was gently layered over the cell suspension. The gradient was centrifuged at 400*g* no brake for 15 min at room temperature. The band of nonparenchymal cell fraction collected was transferred to a new tube, washed twice with HBSS, and centrifuged at 400*g* for 10 min at 4°C to obtain the final pellet. After a step of red blood cell lysis using ACK lysis buffer (Thermo Fisher Scientific), all samples were centrifuged at 1500 rpm for 7 min at 4°C, and the pellets were resuspended in fluorescence-activated cell sorting (FACS) buffer. The samples were divided and transferred to 96-well plates and centrifuged again at 1500 rpm for 7 min at 4°C to pellet cells. Fc receptors were blocked using 5 μg of anti-mouse CD16/32 antibody per sample for 10 min at 4°C. After washing and spinning, the cells were then stained with specific surface markers (see table S2) for 30 min at 4°C, and appropriate isotype antibody and fluorescence minus one (FMO) controls were used. Nonviable cells were labeled using viability dye Ghost Dye red 710. After staining, the cells were washed twice and acquired using a Cytek Aurora spectral cytometer (Cytek Biosceinces) and analyzed using FlowJo software (Tree Star).

E. coli–catching and –killing assay

KCs were isolated after the liver nonparenchymal cell isolation protocol described above. After the red blood cell–lysis step, the cells were resuspended in Dulbecco's modified Eagle's medium (DMEM) containing 10% fetal bovine serum (FBS), and KCs were labeled with anti-mouse F4/80, TIM4, and CRIg. The cells were then washed, resuspended, and counted for normalization among the groups. For the *E. coli*–catching assay, 5×10^6 cells were transferred to six-well low-adherence plates and incubated with mouse serum–opsonized

E. coli in a 1:50 ratio for 1 hour at 37°C under agitation. After, the cells were collected into a new tube, washed, and transferred to FACS tubes for cell acquisition or to 24-well glass bottom plates for imaging. For the *E. coli*–killing assay, 2.5×10^5 cells were transferred to 24-well plastic plates and incubated for 2 hours for cell adhesion. After incubation, the plate wells were washed with cold PBS to remove nonadherent cells, and 5×10^6 mouse serum–opsonized *E. coli* was added to the cells and incubated for 1 hour at 37°C under agitation. The wells were then washed, and 200 μl of DMEM containing 10% FBS and chloramphenicol and tetracycline (30 μg/ml) was added to eliminate the remaining *E. coli*. The antibiotics were incubated for 15 min and washed, and 500 μl of DMEM containing 10% FBS was added to the cells. For in vitro bacterial burden, 500 μl of cell lysis buffer (ddH_2O, 0.1% saponin, and 10 μg/ml of DNAse I) was added to the wells 1 and 4 hours after infection to release the bacteria present inside the KCs. The suspension was collected, transferred to Eppendorf tubes, and centrifuged at 12,000*g* for 2 min. The pellet was resuspended, serial diluted, and plated for CFU counts.

Statistical analysis

The sample size was determined on the basis of experience with similar hypothesis testing experiments. All data are represented as individual values with the means ± SD unless otherwise indicated in the figure legend. In general, each data point is one biological replicate (n). The number of times an experiment was independently repeated (N) and the number of biological replicates (n) are stated in the figure legends. Statistical analyses were performed using GraphPad Prism (Version 8.0). Normality was assessed, and comparisons between two groups were performed using either an unpaired two-tailed Student's t test or the Mann-Whitney test, as appropriate. For comparisons involving three or more groups, one-way analysis of variance (ANOVA) followed by Dunnet's posttest or two-way ANOVA followed by Šidák's posttest was used. Statistical significance is indicated by P values in the figure graphs.

Supplementary Materials

The PDF file includes:
Methods
Figs. S1 to S11
Tables S1 and S2
References (*60*, *61*)

Other Supplementary Material for this manuscript includes the following:
Movies S1 to S4
Data file S1
MDAR Reproducibility Checklist

REFERENCES AND NOTES

1. T. R. Kollmann, B. Kampmann, S. K. Mazmanian, A. Marchant, O. Levy, Protecting the newborn and young infant from infectious diseases: Lessons from immune ontogeny. *Immunity* **46**, 350–363 (2017).
2. S. Oza, J. E. Lawn, D. R. Hogan, C. Mathers, S. N. Cousens, Neonatal cause-of-death estimates for the early and late neonatal periods for 194 countries: 2000–2013. *Bull. World Health Organ.* **93**, 19–28 (2015).
3. C. Fleischmann-Struzek, D. M. Goldfarb, P. Schlattmann, L. J. Schlapbach, K. Reinhart, N. Kissoon, The global burden of paediatric and neonatal sepsis: A systematic review. *Lancet Respir. Med.* **6**, 223–230 (2018).
4. K. E. Rudd, S. C. Johnson, K. M. Agesa, K. A. Shackelford, D. Tsoi, D. R. Kievlan, D. V. Colombara, K. S. Ikuta, N. Kissoon, S. Finfer, C. Fleischmann-Struzek, F. R. Machado, K. K. Reinhart, K. Rowan, C. W. Seymour, R. S. Watson, T. E. West, F. Marinho, S. I. Hay, R. Lozano, A. D. Lopez, D. C. Angus, C. J. L. Murray, M. Naghavi, Global, regional, and national sepsis incidence and mortality, 1990-2017: Analysis for the Global Burden of Disease Study. *Lancet* **395**, 200–211 (2020).
5. J. R. Verani, L. McGee, S. J. Schrag, Division of Bacterial Diseases, National Center for Immunization and Respiratory Diseases, Centers for Disease Control and Prevention (CDC), Prevention of perinatal group B streptococcal disease: Revised guidelines from CDC, 2010. *MMWR Recomm. Rep.* **59**, 1–36 (2010).
6. B. J. Stoll, K. M. Puopolo, N. I. Hansen, P. J. Sánchez, E. F. Bell, W. A. Carlo, C. M. Cotten, C. T. D'Angio, S. N. J. Kazzi, B. B. Poindexter, K. P. Van Meurs, E. C. Hale, M. V. Collins, A. Das, C. J. Baker, M. H. Wyckoff, B. A. Yoder, K. L. Watterberg, M. C. Walsh, U. Devaskar, A. R. Laptook, G. M. Sokol, S. J. Schrag, R. D. Higgins, Eunice Kennedy Shriver National Institute of Child Health and Human Development Neonatal Research Network, Early-onset neonatal sepsis 2015 to 2017, the rise of *Escherichia coli*, and the need for novel prevention strategies. *JAMA Pediatr.* **174**, e200593 (2020).
7. H. Neuman, P. Forsythe, A. Uzan, O. Avni, O. Koren, Antibiotics in early life: Dysbiosis and the damage done. *FEMS Microbiol. Rev.* **42**, 489–499 (2018).
8. S. Shekhar, F. C. Petersen, The dark side of antibiotics: Adverse effects on the infant immune defense against infection. *Front. Pediatr.* **8**, 544460 (2020).
9. H. Huang, J. Jiang, X. Wang, K. Jiang, H. Cao, Exposure to prescribed medication in early life and impacts on gut microbiota and disease development. *EClinicalMedicine* **68**, 102428 (2024).
10. H. S. Deshmukh, Y. Liu, O. R. Menkiti, J. Mei, N. Dai, C. E. O'Leary, P. M. Oliver, J. K. Kolls, J. N. Weiser, G. S. Worthen, The microbiota regulates neutrophil homeostasis and host resistance to *Escherichia coli* K1 sepsis in neonatal mice. *Nat. Med.* **20**, 524–530 (2014).
11. Z. Zeng, B. G. J. Surewaard, C. H. Y. Wong, C. Guettler, B. Petri, R. Burkhard, M. Wyss, H. Le Moual, R. Devinney, G. C. Thompson, J. Blackwood, A. R. Joffe, K. D. McCoy, C. N. Jenne, P. Kubes, Sex-hormone-driven innate antibodies protect females and infants against EPEC infection. *Nat. Immunol.* **19**, 1100–1111 (2018).
12. B. G. J. Surewaard, P. Kubes, Measurement of bacterial capture and phagosome maturation of Kupffer cells by intravital microscopy. *Methods* **128**, 12–19 (2017).
13. Z. Zeng, B. G. J. Surewaard, C. H. Y. Wong, J. A. Geoghegan, C. N. Jenne, P. Kubes, CRIg functions as a macrophage pattern recognition receptor to directly bind and capture blood-borne gram-positive bacteria. *Cell Host Microbe* **20**, 99–106 (2016).
14. M. E. Lopes, B. N. Nakagaki, M. S. Mattos, G. H. Campolina-Silva, R. D. O. Meira, P. H. de Menezes Paixão, A. G. Oliveira, L. D. Faustino, R. Gonçalves, G. B. Menezes, Susceptibility to infections during acute liver injury depends on transient disruption of liver macrophage niche. *Front. Immunol.* **13**, 892114 (2022).
15. D. Zhao, F. Yang, Y. Wang, S. Li, Y. Li, F. Hou, W. Yang, D. Liu, Y. Tao, Q. Li, J. Wang, F. He, L. Tang, ALK1 signaling is required for the homeostasis of Kupffer cells and prevention of bacterial infection. *J. Clin. Invest.* **132**, e150489 (2022).
16. G. Hoeffel, J. Chen, Y. Lavin, D. Low, F. F. Almeida, P. See, A. E. Beaudin, J. Lum, I. Low, E. C. Forsberg, M. Poidinger, F. Zolezzi, A. Larbi, L. G. Ng, J. K. Y. Chan, M. Greter, B. Becher, I. M. Samokhvalov, M. Merad, F. Ginhoux, C-Myb$^+$ erythro-myeloid progenitor-derived fetal monocytes give rise to adult tissue-resident macrophages. *Immunity* **42**, 665–678 (2015).
17. E. Mass, I. Ballesteros, M. Farlik, F. Halbritter, P. Günther, L. Crozet, C. E. Jacome-Galarza, K. Händler, J. Klughammer, Y. Kobayashi, E. Gomez-Perdiguero, J. L. Schultze, M. Beyer, C. Bock, F. Geissmann, Specification of tissue-resident macrophages during organogenesis. *Science* **353**, aaf4238 (2016).
18. C. Schulz, E. G. Perdiguero, L. Chorro, H. Szabo-Rogers, N. Cagnard, K. Kierdorf, M. Prinz, B. Wu, S. E. W. Jacobsen, J. W. Pollard, J. Frampton, K. J. Liu, F. Geissmann, A lineage of myeloid cells independent of Myb and hematopoietic stem cells. *Science* **336**, 86–90 (2012).
19. P. G. Holt, C. A. Jones, The development of the immune system during pregnancy and early life. *Allergy* **55**, 688–697 (2000).
20. D.-M. Popescu, R. A. Botting, E. Stephenson, K. Green, S. Webb, L. Jardine, E. F. Calderbank, K. Polanski, I. Goh, M. Efremova, M. Acres, D. Maunder, P. Vegh, Y. Gitton, J.-E. Park, R. Vento-Tormo, Z. Miao, D. Dixon, R. Rowell, D. McDonald, J. Fletcher, E. Poyner, G. Reynolds, M. Mather, C. Moldovan, L. Mamanova, F. Greig, M. D. Young, K. B. Meyer, S. Lisgo, J. Bacardit, A. Fuller, B. Millar, B. Innes, S. Lindsay, M. J. T. Stubbington, M. S. Kowalczyk, B. Li, O. Ashenberg, M. Tabaka, D. Dionne, T. L. Tickle, M. Slyper, O. Rozenblatt-Rosen, A. Filby, P. Carey, A.-C. Villani, A. Roy, A. Regev, A. Chédotal, I. Roberts, B. Göttgens, S. Behjati, E. Laurenti, S. A. Teichmann, M. Haniffa, Decoding human fetal liver haematopoiesis. *Nature* **574**, 365–371 (2019).
21. W. Li, Y. Wang, H. Zhao, H. Zhang, Y. Xu, S. Wang, X. Guo, Y. Huang, S. Zhang, Y. Han, X. Wu, C. M. Rice, G. Huang, P. G. Gallagher, A. Mendelson, K. Yazdanbakhsh, J. Liu, L. Chen, X. An, Identification and transcriptome analysis of erythroblastic island macrophages. *Blood* **134**, 480–491 (2019).
22. B. G. Lopez, M. S. Tsai, J. L. Baratta, K. J. Longmuir, R. T. Robertson, Characterization of Kupffer cells in livers of developing mice. *Comp. Hepatol.* **10**, 2 (2011).
23. E. Liaskou, D. V. Wilson, Y. H. Oo, Innate immune cells in liver inflammation. *Mediators Inflamm.* **2012**, 949157 (2012).
24. B. McDonald, A. Z. Zucoloto, I.-L. Yu, R. Burkhard, K. Brown, M. B. Geuking, K. D. McCoy, Programing of an intravascular immune firewall by the gut microbiota protects against pathogen dissemination during infection. *Cell Host Microbe* **28**, 660–668.e4 (2020).
25. B. A. David, R. M. Rezende, M. M. Antunes, M. M. Santos, M. A. Freitas Lopes, A. B. Diniz, R. V. Sousa Pereira, S. C. Marchesi, D. M. Alvarenga, B. N. Nakagaki, A. M. Araújo,

D. S. Dos Reis, R. M. Rocha, P. E. Marques, W.-Y. Lee, J. Deniset, P. X. Liew, S. Rubino, L. Cox, V. Pinho, T. M. Cunha, G. R. Fernandes, A. G. Oliveira, M. M. Teixeira, P. Kubes, G. B. Menezes, Combination of mass cytometry and imaging analysis reveals origin, location, and functional repopulation of liver myeloid cells in mice. *Gastroenterology* **151**, 1176–1191 (2016).
26. M. Ershad, A. Mostafa, M. Dela Cruz, D. Vearrier, Neonatal sepsis. *Curr. Emerg. Hosp. Med. Rep.* **7**, 83–90 (2019).
27. J. W. Hommes, B. G. J. Surewaard, Intracellular habitation of *Staphylococcus aureus*: Molecular mechanisms and prospects for antimicrobial therapy. *Biomedicine* **10**, 1804 (2022).
28. Y. Liang, K. Kaneko, B. Xin, J. Lee, X. Sun, K. Zhang, G.-S. Feng, Temporal analyses of postnatal liver development and maturation by single-cell transcriptomics. *Dev. Cell* **57**, 398–414.e5 (2022).
29. C. L. Scott, F. Zheng, P. De Baetselier, L. Martens, Y. Saeys, S. De Prijck, S. Lippens, C. Abels, S. Schoonooghe, G. Raes, N. Devoogdt, B. N. Lambrecht, A. Beschin, M. Guilliams, Bone marrow-derived monocytes give rise to self-renewing and fully differentiated Kupffer cells. *Nat. Commun.* **7**, 10321 (2016).
30. J. Bonnardel, W. T'Jonck, D. Gaublomme, R. Browaeys, C. L. Scott, L. Martens, B. Vanneste, S. De Prijck, S. A. Nedospasov, A. Kremer, E. Van Hamme, P. Borghgraef, W. Toussaint, P. De Bleser, I. Mannaerts, A. Beschin, L. A. Van Grunsven, B. N. Lambrecht, T. Taghon, S. Lippens, D. Elewaut, Y. Saeys, M. Guilliams, Stellate cells, hepatocytes, and endothelial cells imprint the Kupffer cell identity on monocytes colonizing the liver macrophage niche. *Immunity* **51**, 638–654.e9 (2019).
31. A. S. Neupane, M. Willson, A. K. Chojnacki, F. V. E. Silva Castanheira, C. Morehouse, A. Carestia, A. E. Keller, M. Peiseler, A. DiGiandomenico, M. M. Kelly, M. Amrein, C. Jenne, A. Thanabalasuriar, P. Kubes, Patrolling alveolar macrophages conceal bacteria from the immune system to maintain homeostasis. *Cell* **183**, 110–125.e11 (2020).
32. Z. Liu, Y. Gu, S. Chakarov, C. Bleriot, I. Kwok, X. Chen, A. Shin, W. Huang, R. J. Dress, C.-A. Dutertre, A. Schlitzer, J. Chen, L. G. Ng, H. Wang, Z. Liu, B. Su, F. Ginhoux, Fate mapping via Ms4a3-expression history traces monocyte-derived cells. *Cell* **178**, 1509–1525.e19 (2019).
33. A. Gola, M. G. Dorrington, E. Speranza, C. Sala, R. M. Shih, A. J. Radtke, H. S. Wong, A. P. Baptista, J. M. Hernandez, G. Castellani, I. D. C. Fraser, R. N. Germain, Commensal-driven immune zonation of the liver promotes host defence. *Nature* **589**, 131–136 (2021).
34. Y. Miyamoto, J. Kikuta, T. Matsui, T. Hasegawa, K. Fujii, D. Okuzaki, Y. Liu, T. Yoshioka, S. Seno, D. Motooka, Y. Uchida, E. Yamashita, S. Kobayashi, H. Eguchi, E. Morii, K. Tryggvason, T. Shichita, H. Kayama, K. Atarashi, J. Kunisawa, K. Honda, K. Takeda, M. Ishii, Periportal macrophages protect against commensal-driven liver inflammation. *Nature* **629**, 901–909 (2024).
35. G. De Simone, F. Andreata, C. Bleriot, V. Fumagalli, C. Laura, J. M. Garcia-Manteiga, P. Di Lucia, S. Gilotto, X. Ficht, F. F. De Ponti, E. B. Bono, L. Giustini, G. Ambrosi, M. Mainetti, P. Zordan, A. P. Bénéchet, M. Ravà, S. Chakarov, F. Moalli, M. Bajenoff, L. G. Guidotti, F. Ginhoux, M. Iannacone, Identification of a Kupffer cell subset capable of reverting the T cell dysfunction induced by hepatocellular priming. *Immunity* **54**, 2089–2100.e8 (2021).
36. C. Blériot, E. Barreby, G. Dunsmore, R. Ballaire, S. Chakarov, X. Ficht, G. De Simone, F. Andreata, V. Fumagalli, W. Guo, G. Wan, G. Gessain, A. Khalilnezhad, X. M. Zhang, N. Ang, P. Chen, C. Morgantini, V. Azzimato, W. T. Kong, Z. Liu, R. Pai, J. Lum, F. Shihui, I. Low, C. Xu, B. Malleret, M. F. M. Kairi, A. Balachander, O. Cexus, A. Larbi, B. Lee, E. W. Newell, L. G. Ng, W. W. Phoo, R. M. Sobota, A. Sharma, S. W. Howland, J. Chen, M. Bajenoff, L. Yvan-Charvet, N. Venteclef, M. Iannacone, M. Aouadi, F. Ginhoux, A subset of Kupffer cells regulates metabolism through the expression of CD36. *Immunity* **54**, 2101–2116.e6 (2021).
37. F. Sierro, M. Evrard, S. Rizzetto, M. Melino, A. J. Mitchell, M. Florido, L. Beattie, S. B. Walters, S. S. Tay, B. Lu, L. E. Holz, B. Roediger, Y. C. Wong, A. Warren, W. Ritchie, C. McGuffog, W. Weninger, D. G. Le Couteur, F. Ginhoux, W. J. Britton, W. R. Heath, B. M. Saunders, G. W. McCaughan, F. Luciani, K. P. A. MacDonald, L. G. Ng, D. G. Bowen, P. Bertolino, A liver capsular network of monocyte-derived macrophages restricts hepatic dissemination of intraperitoneal bacteria by neutrophil recruitment. *Immunity* **47**, 374–388.e6 (2017).
38. M. Sakai, T. D. Troutman, J. S. Seidman, Z. Ouyang, N. J. Spann, Y. Abe, K. M. Ego, C. M. Bruni, Z. Deng, J. C. M. Schlachetzki, A. Nott, H. Bennett, J. Chang, B. T. Vu, M. P. Pasillas, V. M. Link, L. Texari, S. Heinz, B. M. Thompson, J. G. McDonald, F. Geissmann, C. K. Glass, Liver-derived signals sequentially reprogram myeloid enhancers to initiate and maintain Kupffer cell identity. *Immunity* **51**, 655–670.e8 (2019).
39. S. P. Rosshart, B. G. Vassallo, D. Angeletti, D. S. Hutchinson, A. P. Morgan, K. Takeda, H. D. Hickman, J. A. McCulloch, J. H. Badger, N. J. Ajami, G. Trinchieri, F. Pardo-Manuel De Villena, J. W. Yewdell, B. Rehermann, Wild mouse gut microbiota promotes host fitness and improves disease resistance. *Cell* **171**, 1015–1028.e13 (2017).
40. S. E. Hamilton, T. S. Griffith, A wild microbiome improves mouse modeling of the human immune response. *Lab Anim.* **48**, 337–338 (2019).
41. G. Faure-André, P. Vargas, M.-I. Yuseff, M. Heuzé, J. Diaz, D. Lankar, V. Steri, J. Manry, S. Hugues, F. Vascotto, J. Boulanger, G. Raposo, M.-R. Bono, M. Rosemblatt, M. Piel, A.-M. Lennon-Duménil, Regulation of dendritic cell migration by CD74, the MHC class II-associated invariant chain. *Science* **322**, 1705–1710 (2008).
42. B. McDonald, E. F. McAvoy, F. Lam, V. Gill, C. De La Motte, R. C. Savani, P. Kubes, Interaction of CD44 and hyaluronan is the dominant mechanism for neutrophil sequestration in inflamed liver sinusoids. *J. Exp. Med.* **205**, 915–927 (2008).
43. X. Shi, L. Leng, T. Wang, W. Wang, X. Du, J. Li, C. McDonald, Z. Chen, J. W. Murphy, E. Lolis, P. Noble, W. Knudson, R. Bucala, CD44 is the signaling component of the macrophage migration inhibitory factor-CD74 receptor complex. *Immunity* **25**, 595–606 (2006).
44. S. H. Lee, H. J. Kwon, S. Park, C. I. Kim, H. Ryu, S. S. Kim, J. B. Park, J. T. Kwon, Macrophage migration inhibitory factor (MIF) inhibitor 4-IPP downregulates stemness phenotype and mesenchymal trans-differentiation after irradiation in glioblastoma multiforme. *PLOS ONE* **16**, e0257375 (2021).
45. C. Wang, W. Chen, J. Shen, CXCR7 targeting and its major disease relevance. *Front. Pharmacol.* **9**, 641 (2018).
46. J. Bernhagen, R. Krohn, H. Lue, J. L. Gregory, A. Zernecke, R. R. Koenen, M. Dewor, I. Georgiev, A. Schober, L. Leng, T. Kooistra, G. Fingerle-Rowson, P. Ghezzi, R. Kleemann, S. R. McColl, R. Bucala, M. J. Hickey, C. Weber, MIF is a noncognate ligand of CXC chemokine receptors in inflammatory and atherogenic cell recruitment. *Nat. Med.* **13**, 587–596 (2007).
47. C.-A. Chen, J.-M. Chang, Y.-L. Yang, E.-E. Chang, H.-C. Chen, Macrophage migration inhibitory factor regulates integrin-β1 and cyclin D1 expression via ERK pathway in podocytes. *Biomed. Pharmacother.* **124**, 109892 (2020).
48. N. Paterson, T. Lämmermann, Macrophage network dynamics depend on haptokinesis for optimal local surveillance. *eLife* **11**, e75354 (2022).
49. H. Conroy, L. Mawhinney, S. C. Donnelly, Inflammation and cancer: Macrophage migration inhibitory factor (MIF)—The potential missing link. *QJM* **103**, 831–836 (2010).
50. L. Leng, C. N. Metz, Y. Fang, J. Xu, S. Donnelly, J. Baugh, T. Delohery, Y. Chen, R. A. Mitchell, R. Bucala, MIF signal transduction initiated by binding to CD74. *J. Exp. Med.* **197**, 1467–1476 (2003).
51. E. Gomez Perdiguero, K. Klapproth, C. Schulz, K. Busch, E. Azzoni, L. Crozet, H. Garner, C. Trouillet, M. F. De Bruijn, F. Geissmann, H.-R. Rodewald, Tissue-resident macrophages originate from yolk-sac-derived erythro-myeloid progenitors. *Nature* **518**, 547–551 (2015).
52. B. Brook, D. Harbeson, N. Amenyogbe, R. Ben-Othman, T. R. Kollmann, R. Aniba, Robust health-score based survival prediction for a neonatal mouse model of polymicrobial sepsis. *PLOS ONE* **14**, e0218714 (2019).
53. Y. Y. Pang, J. Schwartz, M. Thoendel, L. W. Ackermann, A. R. Horswill, W. M. Nauseef, agr-Dependent interactions of *Staphylococcus aureus* USA300 with human polymorphonuclear neutrophils. *J. Innate Immun.* **2**, 546–559 (2010).
54. B. G. J. Surewaard, R. Nijland, A. N. Spaan, J. A. W. Kruijtzer, C. J. C. de Haas, J. A. G. van Strijp, Inactivation of staphylococcal phenol soluble modulins by serum lipoprotein particles. *PLOS Pathog.* **8**, e1002606 (2012).
55. L. A. Johnson, S. Banerji, W. Lawrance, U. Gileadi, G. Prota, K. A. Holder, Y. M. Roshorm, T. Hanke, V. Cerundolo, N. W. Gale, D. G. Jackson, Dendritic cells enter lymph vessels by hyaluronan-mediated docking to the endothelial receptor LYVE-1. *Nat. Immunol.* **18**, 762–770 (2017).
56. P. E. Marques, M. M. Antunes, B. A. David, R. V. Pereira, M. M. Teixeira, G. B. Menezes, Imaging liver biology in vivo using conventional confocal microscopy. *Nat. Protoc.* **10**, 258–268 (2015).
57. A. Guillot, M. Kohlhepp, A. Bruneau, F. Heymann, F. Tacke, Deciphering the immune microenvironment on a single archival formalin-fixed paraffin-embedded tissue section by an immediately implementable multiplex fluorescence immunostaining protocol. *Cancer* **12**, 2449 (2020).
58. A. Guillot, M. Winkler, M. Silva Afonso, A. Aggarwal, D. Lopez, H. Berger, M. S. Kohlhepp, H. Liu, B. Özdirik, J. Eschrich, J. Ma, M. Peiseler, F. Heymann, S. Pendem, S. Mahadevan, B. Gao, L. Diehl, R. Gupta, F. Tacke, Mapping the hepatic immune landscape identifies monocytic macrophages as key drivers of steatohepatitis and cholangiopathy progression. *Hepatology* **78**, 150–166 (2023).
59. C. Deppermann, M. Peiseler, J. Zindel, L. Zbytnuik, W.-Y. Lee, E. Pasini, C. Baciu, J. Matelski, Y. Lee, D. Kumar, A. Humar, B. Surewaard, P. Kubes, M. Bhat, Tacrolimus impairs Kupffer cell capacity to control bacteremia: Why transplant recipients are susceptible to infection. *Hepatology* **73**, 1967–1984 (2021).
60. B. Van De Sande, C. Flerin, K. Davie, M. De Waegeneer, G. Hulselmans, S. Aibar, R. Seurinck, W. Saelens, R. Cannoodt, Q. Rouchon, T. Verbeiren, D. De Maeyer, J. Reumers, Y. Saeys, S. Aerts, A scalable SCENIC workflow for single-cell gene regulatory network analysis. *Nat. Protoc.* **15**, 2247–2276 (2020).
61. Z. Gu, R. Eils, M. Schlesner, Complex heatmaps reveal patterns and correlations in multidimensional genomic data. *Bioinformatics* **32**, 2847–2849 (2016).

Acknowledgments: We thank the Kubes laboratory members, especially L. Zbytnuik, M. Wilson, and T. Nussbaumer, for the excellent technical support. We thank the Flow Cytometry core facilities, especially K. Poon, Y. Liu, and R. Maity, for assistance. This study benefited from data generated by Y. Liang and G.-S. Feng. **Funding:** B.A.D. is supported by a Beverly Phillips Rising Star Program Fellowship. F.V.S.C. is supported by a fellowship from the Canadian

Institute of Health Research (MFE-176551). L.S. is supported by a Swiss National Science Foundation (SNSF) research fellowship (#P500PM_203210 and #P5R5PM_225287). M.P. is funded by the Berlin Institute of Health (BIH) clinician scientist program. P.K. is supported by an NSERC Discover grant (RGPIN/07191-2019), the Heart & Stroke Foundation of Canada, CIHR, and the Canada Research Chairs Program. **Author contributions:** Conceptualization: P.K. and B.A.D. Methodology: B.A.D., P.K., A.G., F.V.S.C., M.P., Y.A.A., M.-A.B., B.G.J.S., S.M., J.W.H., and L.S. Formal analysis: B.A.D., J.A., T.Y., A.G., and L.S. Investigation: B.A.D., J.A., A.G., F.V.S.C., M.P., Y.A.A., M.-A.B., B.G.J.S., W.E., S.M., and P.K. Resources: P.K., M.-A.B., B.G.J.S., S.M., F.G., and K.M. Writing: B.A.D. and P.K. Visualization: B.A.D. and P.K. Supervision: P.K. Funding acquisition: P.K. **Competing interests:** The authors declare that they have no competing interests. **Data and materials availability:** The scRNA-seq dataset analyzed in this study was previously published by Liang *et al.* (*28*) and is available in the Gene Expression Omnibus under accession code GSE171993. Tabulated data underlying the figures are provided in data file S1. All data needed to evaluate the conclusions in the paper are present in the paper or the Supplementary Materials. All reagents and materials used in this study are commercially available. Any request for further information should be directed to and will be fulfilled by the first author contact, B.A.D. (bruna.araujodavid@ucalgary.ca). For multiplex immunohistochemistry-related requests, contact A.G. (adrien.guillot@charite.de).

Submitted 8 June 2024
Accepted 27 September 2024
Published 1 November 2024
10.1126/sciimmunol.adq9704